

Glacial-interglacial changes in (H₂O)-O-18, HDO and deuterium excess: results from the fully coupled ECHAM5/MPI-OM Earth system model

Martin Werner, Barbara Haese, Xu Zhang, Martin Butzin, Gerrit Lohmann, Xu Xu

Angaben zur Veröffentlichung / Publication details:

Werner, Martin, Barbara Haese, Xu Zhang, Martin Butzin, Gerrit Lohmann, and Xu Xu. 2016. "Glacial-interglacial changes in (H₂O)-O-18, HDO and deuterium excess: results from the fully coupled ECHAM5/MPI-OM Earth system model." *Geoscientific Model Development* 9 (2): 647–70. <https://doi.org/10.5194/gmd-9-647-2016>.



Glacial–interglacial changes in H_2^{18}O , HDO and deuterium excess – results from the fully coupled ECHAM5/MPI-OM Earth system model

M. Werner¹, B. Haese^{1,2}, X. Xu^{1,3}, X. Zhang¹, M. Butzin¹, and G. Lohmann¹

¹Alfred Wegener Institute, Helmholtz Centre for Polar and Marine Sciences, Bremerhaven, Germany

²Chair for Regional Climate and Hydrology, University of Augsburg, Augsburg, Germany

³Institute of Geosciences, Department of Geology, Kiel University, Kiel, Germany

Correspondence to: M. Werner (martin.werner@awi.de)

Received: 8 August 2015 – Published in Geosci. Model Dev. Discuss.: 16 October 2015

Revised: 22 December 2015 – Accepted: 15 January 2016 – Published: 17 February 2016

Abstract. In this study we present the first results of a new isotope-enabled general circulation model set-up. The model consists of the fully coupled ECHAM5/MPI-OM atmosphere–ocean model, enhanced by the JSBACH interactive land surface scheme and an explicit hydrological discharge scheme to close the global water budget. Stable water isotopes H_2^{18}O and HDO have been incorporated into all relevant model components. Results of two equilibrium simulations under pre-industrial and Last Glacial Maximum conditions are analysed and compared to observational data and paleoclimate records for evaluating the model's performance in simulating spatial and temporal variations in the isotopic composition of the Earth's water cycle. For the pre-industrial climate, many aspects of the simulation results of meteoric waters are in good to very good agreement with both observations and earlier atmosphere-only simulations. The model is capable of adequately simulating the large spread in the isotopic composition of precipitation between low and high latitudes. A comparison to available ocean data also shows a good model–data agreement; however, a strong bias of overly depleted ocean surface waters is detected for the Arctic region. Simulation results under Last Glacial Maximum boundary conditions also fit to the wealth of available isotope records from polar ice cores, speleothems, as well as marine calcite data. Data–model evaluation of the isotopic composition in precipitation reveals a good match of the model results and indicates that the temporal glacial–interglacial isotope–temperature relation was substantially lower than the present spatial gradient for most mid- to high-litudinal regions. As

compared to older atmosphere-only simulations, a remarkable improvement is achieved for the modelling of the deuterium excess signal in Antarctic ice cores. Our simulation results indicate that cool sub-tropical and mid-litudinal sea surface temperatures are key for this progress. A recently discussed revised interpretation of the deuterium excess record of Antarctic ice cores in terms of marine relative humidity changes on glacial–interglacial timescales is not supported by our model results.

1 Introduction

The water cycle is a key component of the Earth's climate system. Documenting and understanding its past evolution is essential to test our ability to model its future changes. Water stable isotopes (H_2^{18}O , HD^{16}O , and H_2^{17}O) are integrated tracers of climate processes occurring in various branches of this cycle (Craig and Gordon, 1965; Dansgaard, 1964). They have been successfully used to describe past climate changes for more than 30 years. For example, water stable isotopes (hereafter expressed in a δ notation as $\delta^{18}\text{O}$ and δD , with respect to the Vienna Standard Mean Ocean Water standard V-SMOW, if not stated otherwise) have been measured routinely over the past decades in polar ice cores (Jouzel, 2013) and more recently also in non-polar ice cores (Hoffmann et al., 2003; Thompson et al., 1998). To a first order, $\delta^{18}\text{O}$ and δD in polar ice cores are used for past temperature reconstructions over the past glacial–interglacial cycles (Jouzel et

al., 2007; NEEM community members, 2013). In addition to high-resolution temperature records, the combination of water isotopic ratios permits one to have a tracer of the low latitudes in polar ice cores (e.g. Stenni et al., 2010; Vimeux et al., 1999). For other (sub)tropical isotope archives, e.g. speleothems, some studies have suggested that the amount of precipitation could be mainly responsible for determining the water isotope concentration (Fleitmann et al., 2003; Wang et al., 2001) – this is called the amount effect (Dansgaard, 1964; Rozanski et al., 1992). Furthermore, in these regions $\delta^{18}\text{O}$ and δD might also reflect convective activity along a moisture trajectory (Vimeux et al., 2005; Yao et al., 2012), changes to regional moisture sources, and the intensity or provenance of atmospheric transport pathways (LeGrande and Schmidt, 2009; Dayem et al., 2010; Lewis et al., 2010; Maher and Thompson, 2012; Caley et al., 2014a; Tan, 2014). High-resolution and well-dated records of $\delta^{18}\text{O}$ of calcite in tropical speleothems in Asia or South America have therefore been interpreted in terms of past monsoon dynamics (Cruz et al., 2005; Wang et al., 2008). Analogously to continental speleothem archives, the seawater oxygen isotope concentration ($\delta^{18}\text{O}_{\text{oce}}$) is conserved in carbonates ($\delta^{18}\text{O}_{\text{c}}$) from corals, foraminifers, and other marine species. Here, temperature during calcite formation and the isotopic composition of the seawater $\delta^{18}\text{O}_{\text{oce}}$ are both the key factors controlling $\delta^{18}\text{O}_{\text{c}}$ (Shackleton, 1974). Thus, carbonate isotope records from ocean sediment cores are fundamental records to access the water mass changes in a different climate. A considerable body of literature shows that they allow the reconstruction of the three-dimensional structure of the ocean when the number of records is sufficient (Caley et al., 2014b; Roche et al., 2014).

As a second-order isotope effect, the deuterium excess – defined as $\text{dex} = \delta\text{D} - 8 \times \delta^{18}\text{O}$ – is a quantity which primarily depends on climatic conditions during evaporative processes (Dansgaard, 1964). According to Merlivat and Jouzel (1979), key parameters that influence the dex signal of the evaporation flux from the ocean surface are both relative humidity above the ocean surface as well as water temperature during evaporation. For many years, it has been assumed that relative humidity remains almost constant during climate changes, and the dex signal of polar ice cores has been used to infer past sea surface temperature changes (Jouzel and Merlivat, 1984; Masson-Delmotte et al., 2005; Steen-Larsen et al., 2014b; Stenni et al., 2001; Vimeux et al., 1999). Recently, Pfahl and Sodemann (2014) have challenged this assumption by arguing that moisture source relative humidity, and not sea surface temperature, is the main driver of dex variability, at least on the present-day seasonal timescale. Their findings are based on the use of an empirical relation between dex and relative humidity together with ERA-Interim reanalysis data (Dee et al., 2011) to globally predict dex values of evaporation fluxes over the ocean. Their results are partly supported by recent monitoring studies of water vapour isotopic composition, which have demonstrated

a strong imprint of source humidity in the North Atlantic on the high deuterium excess of Arctic water vapour (Bonne et al., 2014; Steen-Larsen et al., 2014b, 2013).

However, while direct or indirect records of water isotopes in natural archives provide key documentation of past climate variations, their quantitative translation to climate variables such as temperature or precipitation amount still remains uncertain in many cases. Since the beginning, the interpretation of isotopic time series has been almost entirely based on a modern analogue approach. It is assumed that the observed spatial or seasonal relationship between isotopes and surface temperatures, precipitation amount, or salinity provides a calibration, which is also valid for different climates of the past. This hypothesis was originally supported by the close relationship observed between modern annual mean precipitation isotope values and local annual mean temperature, precipitation amounts, or salinity, and for the atmosphere quantitatively it is consistent with a Rayleigh distillation process. However, this hypothesis is increasingly challenged (i) by new present-day observations and (ii) by alternative paleothermometry methods showing changing relationships for past periods (Buizert et al., 2014; Jouzel, 1999). This calls for a revised understanding of the interpretation of water stable isotopes, including second-order parameters such as deuterium excess, and their relationships with climatic conditions influencing the isotope signal.

One key tool for such an improved understanding of water isotopes in the Earth's hydrological cycle are atmospheric and oceanic general circulation models (GCMs) with an explicit diagnostics of stable water isotopes. During the last 3 decades, several such isotope-enabled GCMs have been built. Such models provide a mechanistic understanding of the physical processes influencing the isotopic composition of different water bodies in the climate system. They allow the explicit simulation of isotopic fractionation processes during any phase changes in a water mass within the model's hydrological cycle, e.g. during evaporation of water from the land or ocean surface, cloud droplet formation, and re-evaporation of droplet water below the cloud base. In such an isotope-enabled GCM set-up, all relevant factors determining the strength and variability of isotopic fractionation are known.

The early implementations of water stable isotopes in atmospheric models (Hoffmann et al., 1998; Joussaume et al., 1984; Jouzel et al., 1987) have already shown their potential in explaining fundamental physical hydroclimate relationships. Since then, considerable progress has been made in simulating stable water isotopes in climate models, as the climate models have evolved themselves (Risi et al., 2010a; Werner et al., 2011). Using atmospheric models, water stable isotopes have been used for a considerable range of applications at small spatial and temporal scales such as investigating the link between water stable isotopes and decadal variability (Kurita et al., 2011) or analysing mixing processes within rain events (Lee et al., 2009; Risi et al., 2010b). Many

of these atmospheric GCMs include at least two stable water isotopes (oxygen-18 and deuterium). With the improvements of the atmospheric GCMs in simulating present-day water isotopic content, part of the interest has lately shifted to second-order content such as deuterium excess and ¹⁷O excess that can provide further constraints on the water cycle but remain challenging (Risi et al., 2010a, 2013; Werner et al., 2011). Besides building atmospheric isotope-enabled GCMs, several international groups have also worked on the inclusion of the water isotopes in oceanic GCMs. Here, the water isotopic content is a passive tracer once the surface oceanic conditions are determined through the water balance with the atmosphere and the additional fractionation during sea-ice formation and melting. Attempts in oceanic-only GCMs have proven useful to challenge the link between oceanic water isotopic content and salinity (Delaygue et al., 2000; Paul et al., 1999; Schmidt, 1998), a subject of considerable interest in paleoceanography.

In general, simulating evolving climate conditions requires using self-contained climate models as much as possible, to avoid prescribing unnecessary or unknown boundary conditions. In particular for past climate applications, it is necessary to simulate stable water isotopes in the full water cycle system, not only in its atmospheric part. As compared to an atmosphere-only or ocean-only set-up, a fully coupled model with an explicit stable water isotope diagnostics will be physically much more consistent regarding relevant fractionation processes during ocean–atmosphere interactions. For past climates, such a coupled isotope model can also generate isotopic compositions in various water reservoirs (e.g. a deuterium excess distribution in ocean surface waters) that are unavailable from proxy data but required as prescribed boundary conditions for uncoupled atmosphere and ocean simulations. So far however, few studies have used fully coupled isotope-enabled climate general circulation models to address questions related to the water cycle. Schmidt et al. (2007) incorporated water isotopes within the water cycle of the Goddard Institute for Space Studies (GISS) coupled ocean–atmosphere model (ModelE). In several multi-centennial simulations, they examined the internal variability and the simulated changes due to orbital and greenhouse gas forcing. Their study was restricted to the modern (pre-industrial) and mid-Holocene (6 kyr BP) climates. LeGrande and Schmidt (2009) expanded these analyses by performing eight Holocene time slice simulations, each ~1000 years apart. Lewis et al. (2010) used the same GISS-E model for simulating the consequences of a large freshwater input into the North Atlantic as an idealized analogue to iceberg discharge during Heinrich events. As a second fully coupled GCM, the HadCM3 model has been enhanced by a stable water isotope diagnostics module by Tindall et al. (2009) for analyses of the present-day isotopic signature of El Niño–Southern Oscillation and the tropical amount effect. Besides these two fully coupled isotope-enabled GCMs, there have also been some efforts in including water stable isotopes in

the hydrological cycle of Earth system models of intermediate complexity (EMICs) by Roche et al. (2004), Brennan et al. (2012), as well as Roche and Caley (2013). These isotope-enabled EMICs can be classified as an alternative tool to test ideas, explore large periods of time in a transient mode, and guide much more computationally demanding simulations with fully coupled GCMs.

The Paleoclimate Modeling Intercomparison Project (PMIP, <http://pmip3.lsce.ipsl.fr>) has chosen the Last Glacial Maximum (LGM) climate as one of the target periods for the evaluation of GCM modelling results. The LGM climate is not only very different from the present and/or pre-industrial climate, but this latest glacial epoch also offers a wealth of terrestrial, marine, and ice core proxy data for an in-depth model–data comparison. As many of these data sets are based on water stable isotopes (e.g. speleothem data, marine calcite data, ice core records), several studies with isotope-enabled GCM have also chosen the LGM as a key period for an evaluation of modelled $\delta^{18}\text{O}$ and δD values with different proxy data (Jouzel et al., 2000; Lee et al., 2008; Lewis et al., 2013; Risi et al., 2010a).

Here we present the first results of a newly developed isotope-enhanced version of the fully coupled ECHAM5/MPI-OM GCM. The model amalgamates our previous efforts to include stable water isotope diagnostics within the ECHAM5 atmosphere GCM (Werner et al., 2011), the JSBACH land surface scheme (Haese et al., 2013), as well as the MPI-OM ocean GCM (Xu et al., 2012). Our following analysis and presentation of simulation results focus on the following questions. (a) How well does this fully coupled Earth system model simulate first-order isotopic variations ($\delta^{18}\text{O}$, δD) within different parts of the Earth's water cycle under pre-industrial and LGM boundary conditions? (b) Do the model results indicate substantial changes in the temperature–isotope relation of meteoric water? (c) Are simulated spatial and temporal variations of the deuterium excess in precipitation, a second-order isotope effect, also in agreement with available observations and paleoproxy data? (d) If so, how are these variations of deuterium excess related to past changes in evaporation processes?

2 Model components and simulation set-up

2.1 Model components

In this study we use the ECHAM5/MPIOM Earth system model, formerly also named community Earth system model COSMOS. It is a fully coupled ocean–atmosphere–sea ice–land surface model (Jungclaus et al., 2006), which has now been enhanced by stable water diagnostics in all relevant model components. Previous studies with the standard (non-isotope) version of ECHAM5/MPI-OM have applied and evaluated this model, among others, for pre-industrial (Wei et al., 2012), glacial, and interglacial climate states (Zhang

et al., 2014, 2013), the Holocene (Wei and Lohmann, 2012), and Cenozoic climate change (Knorr et al., 2011; Stepanek and Lohmann, 2012).

During recent years, all key model components (ECHAM5, MPI-OM, JSBACH) have been equipped with a diagnostic module to explicitly simulate both H₂¹⁸O and HDO within the different parts of the hydrological cycle. Here, we give just a brief summary of key model components and isotope implementation within them and refer to previous publications for details.

The atmosphere component of our model set-up is the ECHAM5 atmosphere GCM, which has mainly been built at the Max Planck Institute for Meteorology, Hamburg. The model has a spectral, dynamical core, which is constrained by the equations of state describing the conservation of mass, energy, and momentum. Further model constraints are set by the continuity equation, a prediction equation for the surface pressure, as well as the hydrostatic equation (Roeckner et al., 2003). The water cycle in ECHAM5 contains formulations for evapotranspiration of terrestrial water, evaporation of ocean water, and the formation of large-scale and convective clouds. Within the atmosphere's advection scheme, vapour, liquid, and frozen water are transported independently. A detailed model description is given in Roeckner et al. (2003, 2006). Stable water isotopes have been implemented in ECHAM5 in an analogous manner to previous ECHAM model releases (Hoffmann et al., 1998; Werner and Heimann, 2002). The isotope module in ECHAM5 computes the isotopic signal of different water masses within the entire water cycle. Details of the implementation have been reported in Werner et al. (2011). In the atmosphere–ocean coupled set-up, ECHAM5 provides the required freshwater flux (P–E) and its isotopic composition for all ocean grid cells to the MPI-OM ocean model.

Within the ECHAM5 model set-up used in this study, the JSBACH land surface model calculates the boundary conditions for ECHAM5 over terrestrial areas. This includes the exchange of water, energy, and momentum between the land surface and the atmosphere (Raddatz et al., 2007). JSBACH divides each land surface grid cell into eight tiles covered by different plant functional types and bare soil. The simulated dynamical vegetation changes are controlled by the processes of natural growing and mortality, as well as disturbance mortality (e.g. wind, fire). Details of this approach are described in Brovkin et al. (2009). The water isotopes H₂¹⁸O and HDO are almost passive tracers in the JSBACH model. No fractionation of the isotopes is assumed during most physical processes partitioning water masses on the land surface (e.g. snowmelt, formation of surface water runoff and drainage; see Haese et al., 2013, for details). For evapotranspiration, fractionation of isotopes might occur during evaporation of water from bare soils. However, the strength of this fractionation remains an open question. In accordance with the results of Haese et al. (2013), we assume in this study that we can ignore any possible fractionation during evapotranspiration

processes from terrestrial areas, as our analyses will focus primarily on the isotopic composition of precipitation. This choice might add a small bias to the isotopic composition of terrestrial surface water pools and the discharge of terrestrial net precipitation (P–E) towards the oceans. Furthermore, it might be relevant for paleoclimate records, where the isotope signal reflects changes in the soil water (e.g. speleothems, ancient groundwater), as a potential fractionation during evapotranspiration processes might lead to substantial changes in the $\delta^{18}\text{O}$ and deuterium excess signal of soil water (Haese et al., 2013). However, it remains an open question whether such changes would also affect the simulated glacial anomalies ($\Delta_{\text{LGM-PI}}\delta^{18}\text{O}$, $\Delta_{\text{LGM-PI}}\text{dex}$), or simply lead to an equivalent strong change in $\delta^{18}\text{O}$ and deuterium excess for both the PI and LGM simulations (without any glacial change).

In the used coupled model set-up, terrestrial water discharge to the ocean is calculated by the so-called Hydrological Discharge scheme (HD scheme; Hagemann and Gates, 2003). Modelled discharge is calculated with respect to the slope of the topography. For the simulated total river runoff it is assumed that the global water cycle is closed, i.e. that all net precipitation (P–E) over terrestrial areas is transported to the ocean. However, lakes are absent in the HD scheme. This may lead to minor errors in the magnitude and location of the modelled river runoff compared to observations. As the ECHAM5/MPI-OM coupled model set-up does not include a dynamic ice sheet model, precipitation amounts falling on glaciers are instantaneously put as runoff into the nearest ocean grid cell to close the global water budget. Independent of the chosen spatial ECHAM5 model resolution, the HD scheme is always implemented on a fine horizontal $0.5^\circ \times 0.5^\circ$ degree grid and allows simulation of water mass flows of the major river systems of the Earth. Stable water isotopes H₂¹⁸O and HDO are incorporated as passive tracers within the HD scheme.

The ocean component of our model set-up consists of the MPIOM general circulation model (Marsland et al., 2003), which is employed on a curvilinear Arakawa-C grid. The used MPIOM set-up has a free surface and contains subgrid-scale parameterizations for convection, vertical and isopycnal diffusivity, horizontal and vertical viscosity, as well as for the bottom boundary layer flow across steep topography. Sea ice is simulated by a viscous-plastic rheology model (Hibler, 1979). It considers thermodynamic sea ice melt and growth, and also a thermohaline coupling by brine rejection. Within MPI-OM, H₂¹⁸O, and HDO are treated as passive tracers. They are fully mixed and advected within the model, and their total mass is conserved. Isotopic variations occur mainly due to temperature-dependent isotope fractionation during evaporation, as well as due to advection and mixing of different water masses. Changes in the oceanic water masses by terrestrial freshwater fluxes entering the ocean are included in the model set-up, too. For the process of sea ice formation from liquid waters, the isotopic composition of sea ice is calculated by a liquid to ice equilibrium fractionation

factor of 1.003, which is the average from various estimates (Craig and Gordon, 1965; Lehmann and Siegenthaler, 1991; Macdonald et al., 1995; Majoube, 1971). Due to the very low rate of isotopic diffusion in sea ice, we assume no fractionation during sea ice melting. In the atmosphere–ocean coupled set-up, MPI-OM provides the isotope composition of sea surface water and sea ice as a temporally varying boundary condition to the ECHAM5 atmosphere model.

Within ECHAM5/MPI-OM, atmosphere and ocean are coupled via the Ocean–Atmosphere–Sea Ice–Soil (OASIS3) coupler (Valcke et al., 2003). Mass, energy, and momentum fluxes, as well as the related isotope masses of H₂¹⁸O and HDO, are exchanged between the atmosphere and ocean once per day. The coupling is described in detail in Jungclauss et al. (2006).

2.2 Simulation set-up

We have used the following simulation set-up for all simulation results presented in this study: the ECHAM5 atmospheric component runs at a horizontal resolution of approx. $3.75^\circ \times 3.75^\circ$ with 19 vertical levels between the surface and 10 hPa (T31L19 resolution). The same horizontal resolution is applied for the JSBACH land surface scheme. The MPI-OM ocean model has a formal horizontal resolution of approx. $3^\circ \times 1.8^\circ$ and 40 uneven vertical layers on z levels. The used MPI-OM model set-up has a bipolar orthogonal spherical coordinate system, where the poles are placed over Greenland and Antarctica, respectively. Placing one pole over Greenland avoids a grid singularity in the Arctic Ocean. Furthermore, it ensures a high horizontal grid resolution in the deep-water formation regions of the northern North Atlantic Ocean and the Arctic.

Two different simulations were performed, one for the pre-industrial and one for the LGM climate. We briefly describe here these experimental set-ups: for the pre-industrial (PI) climate, ECHAM5/MPI-OM has been continued from a PI simulation without isotopes included, which has been run into equilibrium over several thousand years (Wei et al., 2012; Zhang et al., 2013) using identical PI boundary conditions. At model start, isotope values in the atmosphere were set to constant values ($\delta^{18}\text{O}$: -10‰ ; δD : -80‰), while the oceanic isotope distribution was taken from an equilibrium run over 3000 years with the MPI-OM-wiso ocean model (Xu, 2012) with global mean $\delta^{18}\text{O}$ and δD values of 0‰ each (Baertschi, 1976; de Wit et al., 1980). The fully coupled ECHAM5/MPI-OM model with included isotope diagnostics was then run under PI boundary conditions (orbital forcing, greenhouse gas concentrations, ocean bathymetry, land surface and ice sheet topography) for another 1500 years. For the LGM simulation, we impose orbital forcing and greenhouse gas concentrations ($\text{CO}_2 = 185\text{ ppm}$; $\text{N}_2\text{O} = 200\text{ ppb}$; $\text{CH}_4 = 350\text{ ppb}$) as well as surface boundary conditions (terrestrial topography, ocean bathymetry, runoff routes according to ice sheet reconstruction) in accordance

with the PMIP3 protocol (<http://pmip3.lsce.ipsl.fr/>). An increased global salinity (1 PSU added compared to modern values) accounts for a LGM sea level drop of approx. 116 m. Again, the isotope-enabled version of ECHAM5/MPI-OM has been restarted from an already equilibrated simulation without isotopes (Zhang et al., 2013). The initial LGM oceanic H₂¹⁸O and HDO distribution has been taken from a 3000-year long MPI-OM-wiso integration under LGM boundary conditions (Xu, 2012) with a prescribed glacial increase in $\delta^{18}\text{O}$ of $+1\text{‰}$. As in previous uncoupled studies (e.g. Risi et al., 2010a; Werner et al., 2001) we assume no glacial change in the mean deuterium excess in the ocean, which implies a glacial change in δD of $+8\text{‰}$. The fully coupled ECHAM5/MPI-OM model with included isotope diagnostics was then run for another 1500 years.

At the end of the PI and LGM simulation period, none of the two runs shows any trend in the isotopic composition of ocean surface waters, and $\delta^{18}\text{O}$ (δD) trends in deep ocean waters at 2200 m are smaller than $0.005\text{‰}/100\text{ years}$ ($0.05\text{‰}/100\text{ years}$). Thus, we rate both simulations as equilibrated and consider the last 100 model years for our analyses.

If not stated otherwise, all reported δ values of meteoric waters (precipitation, evaporation) in this study are calculated as precipitation- (or evaporation)-weighted averages with respect to the V-SMOW scale. The δ values of ocean waters are calculated as arithmetic averages with respect to the V-SMOW scale.

3 Observational data

3.1 GNIP and GISS database

The Global Network of Isotopes in Precipitation (GNIP) was initiated in 1958 by IAEA and WMO, and became operational in 1961 (IAEA/WMO, 2010). Since then, monthly samples of H₂¹⁸O and HDO in precipitation have been sampled at more than 900 stations from more than 100 different countries. While several stations have continuously collected samples for 2 or more decades (e.g. GNIP stations in Krakow, Ottawa, Reykjavik, and Vienna), many other GNIP stations have been in operation for a much shorter period, only. Here, we use a subset of 70 stations from the GNIP database, where surface temperature, precipitation, $\delta^{18}\text{O}$, and δD have been reported for a minimum of 5 calendar years, any time within the period 1961 to 2007.

The GISS global seawater oxygen-18 database (Schmidt et al., 1999) is a collection of over 26 000 seawater ¹⁸O values made since about 1950. Partial versions of this database already appeared in Schmidt (1999) and Bigg and Rohling (2000). From this database we are using only values with no applied correction (see Schmidt et al., 1999, for details of the applied corrections). It is important to note that, in contrast to GNIP $\delta^{18}\text{O}$ values of precipitation, GISS $\delta^{18}\text{O}$ values in ocean water do not represent annual mean values,

Table 1. Selected ice core records, reported PI and $\Delta(\text{LGM-PI})$ values of $\delta^{18}\text{O}$ and deuterium excess (dex). No correction for glacial $\delta^{18}\text{O}$ enrichment has been applied to the listed ice core values. All values are given in permil on the SMOW scale.

Site	Lon	Lat	$\delta^{18}\text{O}_{\text{PI}}$	dex _{PI}	$\Delta\delta^{18}\text{O}_{\text{LGM-PI}}$	$\Delta\text{dex}_{\text{LGM-PI}}$
Vostok ^{a,b}	106.87	−78.47	−57	15.5	−4	−3
Dome F ^{b,c}	39.70	−77.32	−55	14	−4	−2.5
Dome B ^a	94.92	−77.08	−55	13.5	−5	−
EDC ^{a,d}	123.35	−75.10	−50.9	8.9	−5.4	−3.2
EDML ^{c,d}	0.07	−75.00	−44.9	4.5	−5	−2.9
Taylor Dome ^a	158.72	−77.80	−38.9	4.9	−3	−
Talos ^c	159.18	−72.82	−37.5	3.9	−5	−
Byrd ^a	−119.52	−80.02	−32.9	4.5	−8	−
Siple Dome ^c	−148.82	−81.67	−26.9	2.9	−8	−
WDC ^c	−112.14	−79.46	−34	−	−8	−
GRIP ^a	−37.63	72.58	−35	9.5	−7	−3
NGRIP ^{a,e}	−42.32	75.10	−35.2	−	−8	−
NEEM ^f	−51.06	77.45	−	−	−7.5	−
Camp Century ^{a,g}	−61.13	77.17	−28	−	−12.9	−
Dye3 ^h	−43.81	65.18	−30	−	−5.5	−
Renland ^{a,h}	−25.00	72.00	−26.5	−	−5	−
Huascaran ^a	−77.61	−9.11	−	−	−6.3	−4
Sajama ^a	−68.97	−18.10	−	−	−5.4	−
Illimani ^a	−67.77	−16.62	−	−	−6	−4
Guliyá ^a	81.48	35.28	−	−	−5.4	−
Dunde ^a	96.00	38.00	−	−	−2	−

References: ^a reported in Risi et al. (2010a), ^b Uemura et al. (2012), ^c WAIS Divide project members (2013), ^d Stenni et al. (2010), ^e North Greenland Ice Core project members (2004), ^f NEEM community members (2013), ^g Johnsen et al. (1972), ^h Johnsen et al. (2001).

but are typically measured from a sample taken during an arbitrary day of the year. Therefore, we compare in this study the GISS data not to simulated annual mean isotope values in ocean waters, but to the long-term mean monthly value of the specific month, when a GISS $\delta^{18}\text{O}$ value was reported.

3.2 Ice core data

In the late 1960s Dansgaard et al. (1969), Lorius et al. (1979) and others started their pioneering work of analysing polar ice cores for climate research. Since then, the isotopic composition of more than a dozen deep ice cores both from Greenland and Antarctica has been measured. In parallel, alpine ice cores from (sub)tropical regions of South America (Hoffmann et al., 2003; Thompson et al., 1995), Africa (Thompson et al., 2002) and the Tibetan Plateau (Thompson et al., 1989; Tian et al., 2003; Yao et al., 2012) have been drilled and analysed during the last decades too. In this study we use a subset of 6 Greenland, 10 Antarctic, and 5 (sub)tropical ice cores to compare the measured $\delta^{18}\text{O}$ and δD values for the pre-industrial climate and the LGM with our simulation results. For the different ice core records, we take the minimum $\delta^{18}\text{O}$ (δD , dex) value of the time interval 19 000 to 23 000 years BP as a representative mean LGM $\delta^{18}\text{O}$ (δD , dex) value. The ice core data used in this study are summarized in Table 1.

3.3 Speleothem calcite data

Recently, Shah et al. (2013) published a global synthesis of speleothem $\delta^{18}\text{O}$ records spanning the period from the LGM until the present, which consists of data from 60 speleothems of 36 different sites. From this compilation we have selected a subset of eight speleothem records (Table 2), where 1000 year averaged $\delta^{18}\text{O}$ values calculated by Shah et al. (2013) are available for both the LGM (defined here as the period 19 000 to 22 000 years BP) and the most recent 1000 years BP. We use the latter as representative mean PI $\delta^{18}\text{O}$ values at the different locations. We are aware that during the last 1000 years BP the climate at a specific speleothem site might have been variable and different from the pre-industrial climate of our ECHAM5/MPI-OM simulation, which could lead to a bias in the model–data comparison. We are also aware that drip water in a cave, whose isotopic composition is archived in a speleothem record, might be seasonally biased due to re-evaporation of the precipitated water (Wackerbarth et al., 2010). Furthermore, for many speleothems, an additional fractionation between the drip water and the formed calcite can be observed (Dreybrodt and Scholz, 2011). Thus, necessary caution will be taken for the comparison of model results of $\delta^{18}\text{O}$ in precipitation with the selected speleothem data.

Table 2. Selected speleothem sites, reported PI and LGM values of $\delta^{18}\text{O}_\text{c}$ in calcite, and the calculated LGM-PI $\Delta\delta^{18}\text{O}_{\text{c,LGM-PI}}$ change. All values have been taken from a compilation by Shah et al. (2013) and represent 1000 year averaged $\delta^{18}\text{O}_\text{c}$ values for both the LGM (defined here as the period from 19 000 to 22 000 years BP) and the most recent 1000 years BP (used as an estimate for $\delta^{18}\text{O}_{\text{c,PI}}$). For Botuverá Cave, Gunung Buda National Park, and Sanbao Cave, mean values of several reported speleothem records have been calculated. All $\delta^{18}\text{O}_\text{c}$ values refer to the PDB standard.

Cave name	Lon	Lat	$\delta^{18}\text{O}_{\text{c,PI}}$ (‰)	$\Delta\delta^{18}\text{O}_{\text{c,LGM-PI}}$ (‰)
Botuverá	−49.16	−27.22	−3.2	−0.3
Cold Air	29.11	−24.02	−4.3	1.2
Gunung Buda	114.80	4.03	−9.3	1.7
Jerusalem West	35.15	31.78	−4.9	1.4
NWSI	172.00	−42.00	−3.2	0.3
Sanbao	110.43	31.67	−8.8	0.1
Sofular	31.93	41.42	−8.1	−4.5
Soreq	35.03	31.45	−5.4	2.2

All listed $\delta^{18}\text{O}$ data in Table 2 are measured isotope values in carbonate and refer to the Pee Dee Belemnite (PDB) standard. For comparison with model results, $\delta^{18}\text{O}$ values in calcite are converted between the PDB and SMOW scale as the following (Coplen et al., 1983; Sharp, 2007):

$$\delta^{18}\text{O}_{\text{c(PDB)}} = 0.97002 \times \delta^{18}\text{O}_{\text{c(SMOW)}} - 29.98.$$

For an estimation of $\delta^{18}\text{O}$ in the drip water, we apply a formula linking $\delta^{18}\text{O}$ in water and $\delta^{18}\text{O}$ in speleothem calcite, derived by Kim and O’Neil (1997) for synthetic calcite:

$$\delta^{18}\text{O}_{\text{c(SMOW)}} = \delta^{18}\text{O}_{\text{water(SMOW)}} + 18.03 \times \frac{1000}{T} - 32.42 + 0.27,$$

with T being the temperature (in Kelvin) during calcite formation. As mentioned above, we further assume that the $\delta^{18}\text{O}$ values in drip water, calculated in such a way, are a reliable proxy for the annual mean $\delta^{18}\text{O}$ in precipitation falling at the cave site, and can thus be directly compared to our model results.

3.4 Marine calcite data

Caley et al. (2014b) recently compiled and published a marine calcite $\delta^{18}\text{O}$ data set from 114 (115) pairs of deep-sea cores, which contain both LGM and Late Holocene planktic (benthic) foraminifera $\delta^{18}\text{O}$ data. In their study they report $\delta^{18}\text{O}$ anomalies as the change between mean $\delta^{18}\text{O}$ values of the period 19 000 to 23 000 years BP and over the last 3000 years of each record. The MARGO project definition has been used to ensure the chronostratigraphic quality of the selected data (Kucera et al., 2005). Planktic foraminifera data have been mainly measured in the following species: *Globigerinoides sacculifer*, *Globigerinoides ruber pink* and *white*, *Neoglobobulimina pachyderma sinistral*, and *Globigerina bulloides*. Benthic foraminifera data include, among

others, *Cibicidoides wuellerstorfi*, *Cibicidoides pachyderma*, and *Cibicidoides peregrina*. For a more detailed description of this data set, we refer the reader to Caley et al. (2014b).

According to Shackleton (1974), the $\delta^{18}\text{O}_\text{c}$ signal in calcite shells of planktic and benthic foraminifera can be interpreted by the following expression relating temperature to the equilibrium fractionation of inorganic calcite precipitation around 16.9 °C:

$$T = 16.9 - 4.38 \times \left(\delta^{18}\text{O}_{\text{c(PDB)}} - \delta^{18}\text{O}_{\text{oce(PDB)}} \right) + 0.1 \times \left(\delta^{18}\text{O}_{\text{c(PDB)}} - \delta^{18}\text{O}_{\text{oce(PDB)}} \right)^2,$$

with T being the temperature during calcite formation, $\delta^{18}\text{O}_{\text{c(PDB)}}$ the isotopic composition of calcite on the PDB scale, and $\delta^{18}\text{O}_{\text{oce(SMOW)}}$ the isotopic composition of seawater on the SMOW scale. The conversion between the PDB and SMOW isotope scales can be expressed as $\delta^{18}\text{O}_{\text{oce(PDB)}} = \delta^{18}\text{O}_{\text{oce(VSMOW)}} - 0.27$ (Hut, 1987).

4 Results and discussion

4.1 Present-day model evaluation

4.1.1 Isotopes in precipitation

Figure 1a shows the global distribution of annual mean $\delta^{18}\text{O}$ values in precipitation ($\delta^{18}\text{O}_\text{p}$) as simulated by the ECHAM5/MPI-OM model with isotope diagnostics included. As for a comparable simulation with the ECHAM5-wiso atmosphere-only model (Werner et al., 2011), all major characteristics of the global H₂¹⁸O distribution in precipitation as previously reported by Dansgaard (1964) can be found in the global map of $\delta^{18}\text{O}_\text{p}$. In general, depletion of $\delta^{18}\text{O}_\text{p}$ is seen in mid- to high-latitude regions as compared to values in the low latitudes (temperature effect). The strongest depletion of $\delta^{18}\text{O}_\text{p}$ (down to −54 ‰) occurs over the po-

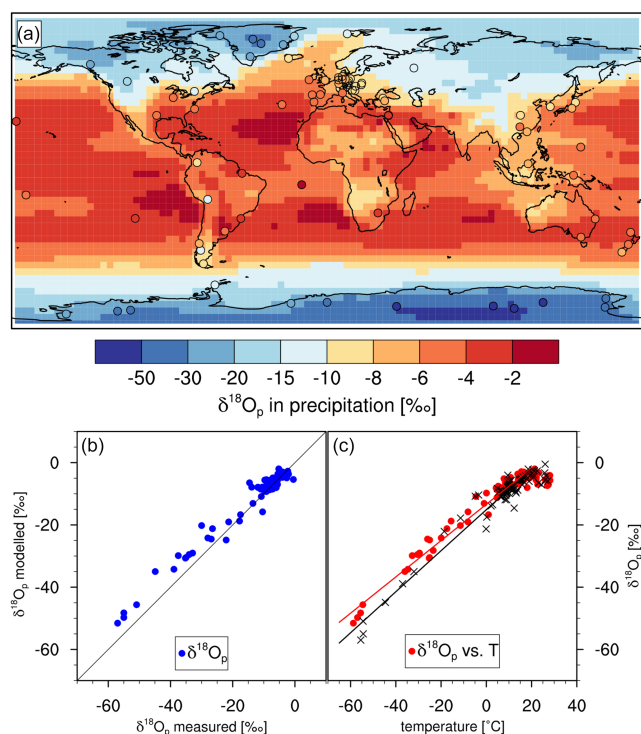


Figure 1. (a) Global distribution of simulated and observed annual mean $\delta^{18}\text{O}_p$ values in precipitation. The background pattern shows the $\delta^{18}\text{O}_p$ distribution as simulated by the ECHAM5/MPI-OM model set-up. Data from 70 GNIP stations (see text), from 21 ice core records (Table 1) and from 8 speleothem records (Table 2) are plotted as coloured symbols. (b) Modelled vs. observed annual mean $\delta^{18}\text{O}_p$ at the different GNIP, speleothem, and ice core sites. The black line represents the 1 : 1 line indicating a perfect model fit. (c) Observed (black crosses) and modelled (filled red circles) spatial $\delta^{18}\text{O}_p$ – T relationship for annual mean values of T and $\delta^{18}\text{O}_p$ at 71 sites, where observed annual mean temperatures are below $+20^\circ\text{C}$. The black (red) solid line represents a linear fit of the observed (modelled) data set.

lar ice sheets of Antarctica and Greenland. A longitudinal gradient of isotopic depletion in precipitation is simulated from the Atlantic Ocean towards Europe and Eurasia and towards eastern North America (continental effect). Strongly depleted $\delta^{18}\text{O}_p$ values are also found over alpine mountain regions like the Andes and the Tibetan Plateau (altitude effect).

For a more quantitative evaluation of the model results, we compare the simulated annual mean $\delta^{18}\text{O}_p$ values with observational data from the selected 70 GNIP stations, 21 ice cores, and 8 speleothems (Sect. 3). To convert the reported speleothem PI values of $\delta^{18}\text{O}_c$ in calcite (Table 2) to $\delta^{18}\text{O}_p$ in precipitated water, we apply the formulae given in Sect. 3.3. For the required site temperatures, we have interpolated annual mean ERA40 soil temperatures (layer no. 1, mean of the period 1961–1990) to the different speleothem sites. We find that the modelled $\delta^{18}\text{O}_p$ values are in good agreement with

the observational data, with a linear correlation coefficient r^2 of 0.97, and a root mean square error (RMSE) of 3.0‰ between measured and modelled $\delta^{18}\text{O}_p$ values (Fig. 1b). For an evaluation of the modelled temperature effect (Fig. 1c), we focus on the 71 data sets in mid- to high-latitude regions with an annual mean temperature value below 20°C . The modelled global $\delta^{18}\text{O}$ – T gradient ($0.58\text{‰}/^\circ\text{C}$; $r^2 = 0.96$) is close to the observed gradient ($0.66\text{‰}/^\circ\text{C}$; $r^2 = 0.95$), with main deviations caused by an underestimation of depletion for cold regions with mean temperatures below -20°C . This result is similar to the findings for the ECHAM5-wiso atmosphere model, and the deviations can partly be explained by the coarse T31L19 model resolution (Werner et al., 2011). Similar distributions of $\delta^{18}\text{O}$ and δD in precipitation have been reported for several atmosphere-only and fully coupled GCMs during the last years (e.g. Lee et al., 2007; Risi et al., 2010a; Schmidt et al., 2007; Tindall et al., 2009). While all these models show a reasonable resemblance to GNIP observations for the large-scale patterns in low- and mid-latitude regions, some models have difficulties in correctly simulating the very low temperatures and strong isotope depletions over the Antarctic ice sheet (e.g. Lee et al., 2007).

4.1.2 Isotopes in ocean waters

In Fig. 2a, the simulated annual mean $\delta^{18}\text{O}_{\text{oce}}$ signal in ocean surface waters (mean over the depth interval between the surface and 10 m) are plotted. Mean values in the tropical to mid-latitude oceans range between $+0.05$ and $+1.2\text{‰}$, with a tendency to higher values in the Atlantic Ocean as compared to the Pacific and Indian oceans. This relative enrichment can be explained by a net freshwater export of Atlantic Ocean water, which is transported westwards to the Pacific (Broecker et al., 1990; Lohmann, 2003; Zaucker and Broecker, 1992). The highest enrichment in the Atlantic Ocean is found south of Bermuda, with surface water $\delta^{18}\text{O}_{\text{oce}}$ values of up to $+1.3\text{‰}$. Other, more localized regions of surface water $\delta^{18}\text{O}_{\text{oce}}$ enrichment with a similar order of magnitude are the Mediterranean Sea, the Black Sea, as well as the Red Sea. Again, this enrichment is most likely caused by a regional surplus of evaporation vs. precipitation in these three regions. Stronger than average depletion of $\delta^{18}\text{O}_{\text{oce}}$ surface waters is simulated for both high-latitude ocean regions. While surface waters in the Southern Ocean between 50 and 75°S show a depletion of down to -0.8‰ , modelled surface waters in the Arctic Ocean are depleted by down to -1.6‰ . This depletion is most likely caused by two effects: (a) the implemented fractionation during sea-ice formation which leads to an enrichment (depletion) of the isotopes in sea ice (the remaining liquid water); and (b) the inflow of highly depleted water masses of Arctic rivers in combination with a strong stratification of the simulated Arctic Ocean water masses (see below).

For a quantitative evaluation of the model results, we compare the simulated values to 3859 $\delta^{18}\text{O}$ entries of the selected

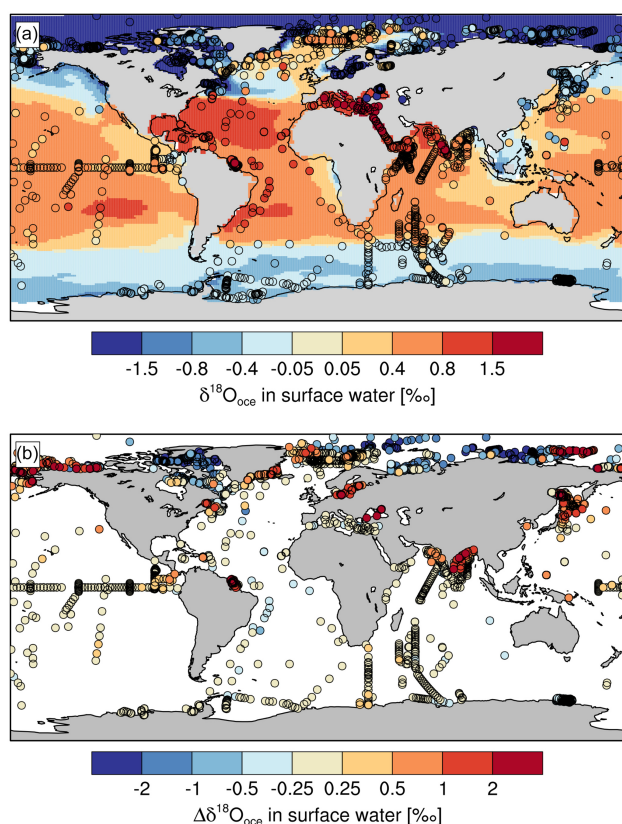


Figure 2. (a) Global distribution of simulated and observed annual mean $\delta^{18}\text{O}_{\text{oce}}$ values in ocean surface waters (mean over the depth interval between surface and 10 m). The background pattern shows the $\delta^{18}\text{O}_{\text{oce}}$ distribution as simulated by the ECHAM5/MPI-OM model set-up. Data entries from the GISS database are plotted as coloured symbols. (b) Anomaly plot for the difference of the mean modelled vs. observational values ($\Delta\delta^{18}\text{O}_{\text{oce}} = \delta^{18}\text{O}_{\text{oce}} - \delta^{18}\text{O}_{\text{GISS}}$) at the positions of the GISS data entries. For the calculation of $\Delta\delta^{18}\text{O}_{\text{oce}}$, the month of sampling has been considered (see text for details).

GISS data (Sect. 3.1), which represent surface ocean water values between the surface and 10 m depth. On a global scale, the simulated $\delta^{18}\text{O}_{\text{oce}}$ values agree quite well within a range of ± 0.25 ‰ with the GISS values (Fig. 2b). The strongest model–data deviations are found in the following regions: (a) in the vicinity of several large river estuaries, the model results reveal overly high $\delta^{18}\text{O}_{\text{oce}}$ values (e.g. at the Amazon and Ganges river mouths); (b) the model also overestimates $\delta^{18}\text{O}_{\text{oce}}$ in surface water in the Baltic Sea as well as in the Black Sea; and (c) for the Arctic Ocean region, the comparison yields mixed results: while the MPI-OM model tends to overestimate $\delta^{18}\text{O}_{\text{oce}}$ in ocean surface waters in some regions by more than $+2$ ‰ (e.g. the eastern coast of Greenland, and in the Beaufort Sea north of Alaska), in most other Arctic regions the model results are lower by more than -2 ‰ than the GISS observations (e.g. in the Hudson Bay area, the Barents Sea, the Kara Sea, as well as the Laptev Sea).

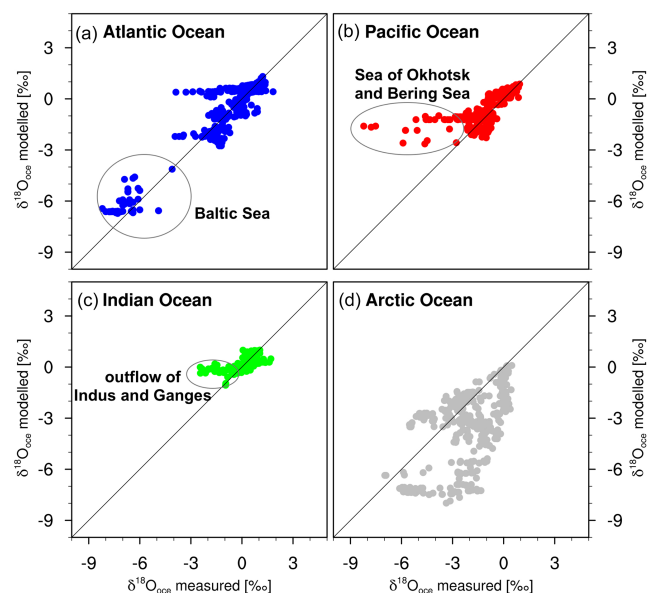


Figure 3. Scatter plots of observed present-day $\delta^{18}\text{O}_{\text{oce}}$ values from the GISS database vs. modelled $\delta^{18}\text{O}_{\text{oce}}$ values of the PI simulation for the following basins: (a) Atlantic Ocean, (b) Pacific Ocean, (c) Indian Ocean, and (d) Arctic Ocean. The black lines represent the 1 : 1 line, indicating a perfect model fit.

A separation of the model–data comparison into the Atlantic, Pacific, Indian, and Arctic oceans does not show any systematic deviations between modelled $\delta^{18}\text{O}_{\text{oce}}$ values and the GISS data for the first three oceans (Fig. 3). We find strong correlations between modelled values and the GISS data as well as a RMSE below 1 ‰ for all three oceans (Atlantic: $n = 458$, $r^2 = 0.91$, RMSE = 0.77; Pacific: $n = 736$, $r^2 = 0.60$, RMSE = 0.75; Indian Ocean: $n = 345$, $r^2 = 0.46$, RMSE = 0.46). The strongest deviations of model values from observational data are caused by the overestimation of $\delta^{18}\text{O}_{\text{oce}}$ values near river estuaries, at the Baltic Sea, and at the Sea of Okhotsk. For the Arctic Ocean, the majority of the simulated $\delta^{18}\text{O}_{\text{oce}}$ values are more strongly depleted than the corresponding GISS entries, and the model–data correlation is worse ($n = 410$, $r^2 = 0.33$, RMSE = 2.25). This bias in our ECHAM5/MPI-OM model is most likely caused by an overly stratified Arctic Ocean. Highly depleted water inflowing from Arctic rivers remains in the upper layers of the Arctic Ocean and is not well mixed with deeper waters. This model deficit is clearly depicted in a comparison of the mean modelled isotope signal with available measurements from the GISS database in meridional sections of the Atlantic (zonal mean between 60 and 0° W; Fig. 4a, c) and the Pacific basin (zonal mean of region 150° E to 110° W; Fig. 4b, d). For both cross sections, we find that the overestimated depletion of $\delta^{18}\text{O}_{\text{oce}}$ values in the Arctic reaches down to approx. 500 m below the surface, while simulated North Atlantic Deep Water (NADW) masses are less depleted and in better agreement with the GISS data. Similar low isotope val-

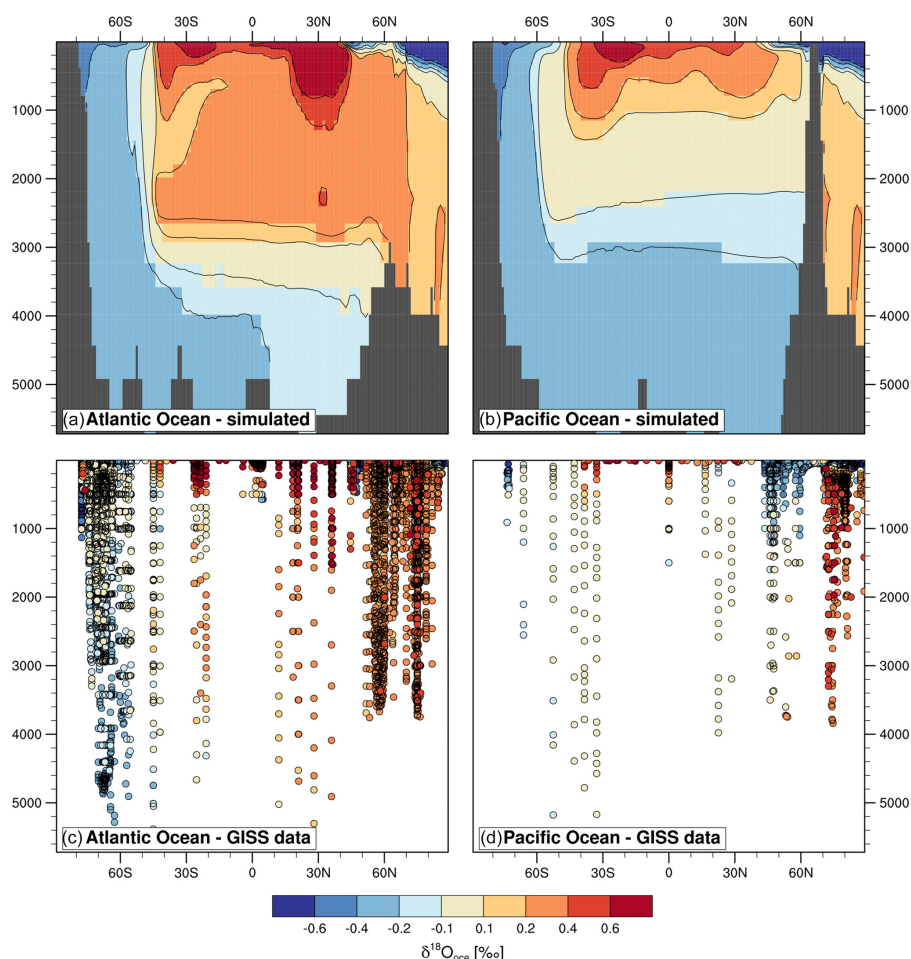


Figure 4. Meridional section of the simulated $\delta^{18}\text{O}_{\text{oce}}$ values in (a) the Atlantic (zonal mean over 60 to 0° W) and (b) the Pacific (zonal mean over 150° E to 110° W). Data entries from the GISS database for the same regions (Atlantic Ocean: $n = 5811$; Pacific Ocean: $n = 2985$) are plotted as coloured symbols in panels (c) and (d).

ues in the Arctic Ocean have already been reported by former studies with ocean-only GCMs (Paul et al., 1999; Xu et al., 2012).

In general, we find for the Atlantic Ocean a fair agreement between GISS observations and model values. The regions of the strongest enrichment are located between 40° S and 30° N, with maximum enrichment (+0.6 ‰ or more) at approx. 20° S and 30° N, and a decreasing trend of enrichment in deeper water until approx. +0.1 ‰ at a depth of 3000 m. The enriched water masses are also found in NADW below 1000 m, with an enrichment of up to +0.2 ‰ (Fig. 4a). On the contrary, Atlantic water masses south of 40° S show a relative depletion down to −0.4 ‰ in their isotopic signature for all water depths, in agreement with available GISS data (Fig. 4c). Depleted water masses stemming from the Antarctic Bottom Water (AABW) reach until the Equator, where the isotopic signal is then mixed with NADW and enriched tropical Atlantic waters. For the Pacific (Fig. 4b), we find a similar vertical and latitudinal $\delta^{18}\text{O}_{\text{oce}}$ distribution as in the upper

layers of the Atlantic Ocean, with the transition zone between enrichment and depletion ascended to approx. 1000 m water depth. Below a depth of approx. 3500 m, depleted AABW ($\delta^{18}\text{O}_{\text{oce}}$ between −0.4 and −0.1 ‰) fills the entire Pacific. The overall pattern of the Atlantic and Pacific cross sections is in good agreement with a recent study of the *i*LOVECLIM isotope-enabled EMIC (Roche and Caley, 2013) as well as with two ocean-only GCM studies (Paul et al., 1999; Xu et al., 2012).

4.1.3 Discharge of terrestrial surface water

In Fig. 5a, we show the simulated annual mean values of $\delta^{18}\text{O}$ for grid cells with a mean inflow of at least $200 \text{ m}^3 \text{ s}^{-1}$, as simulated by the HD scheme (see Sect. 2.1), to depict the major river systems on Earth only. In general, the isotopic composition of a specific river is closely linked to the $\delta^{18}\text{O}$ signal of P–E in the catchment area of the particular river. The strongest depletion of down to −12 ‰ is found for river

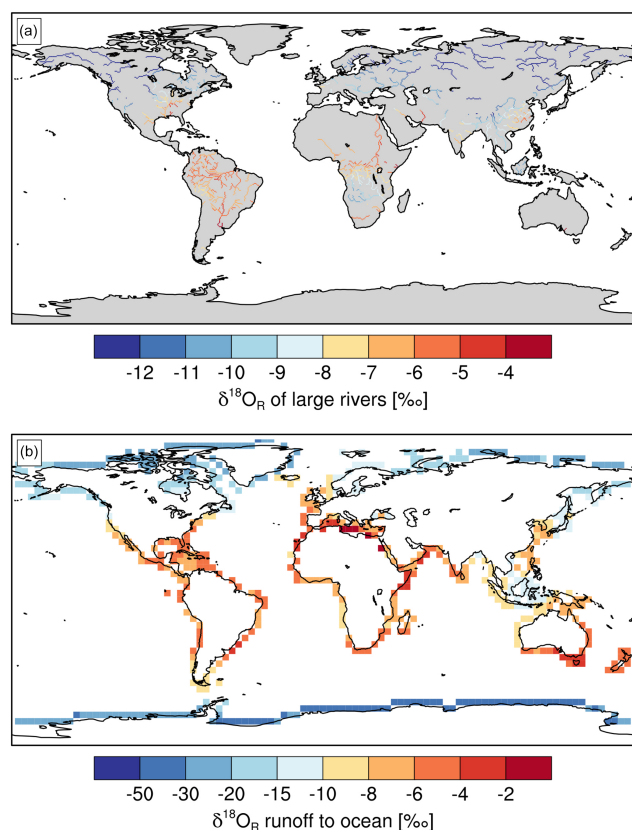


Figure 5. Global distribution of the simulated annual mean $\delta^{18}\text{O}_R$ signal in (a) large rivers and (b) surface water runoff from coastal grid points into the oceans, as simulated by the hydrological discharge model (HD model) within the ECHAM5/MPI-OM set-up.

systems of high northern regions of Siberia and Alaska, in agreement with observational data (Dodd et al., 2012). For the Rhine, the simulated isotopic composition in the Netherlands is about -7 to -8 ‰, in good agreement with available observations, and similar good agreement is found for the Mackenzie River in the Canadian Arctic with a modelled outflow signal of -19 to -20 ‰ (Hoffmann et al., 1998). Rivers in middle and low latitudes contain in general more enriched waters, and the PI model experiment results in the least depleted waters (> -4 ‰) for the Paraná River (Argentina) and the Orange River (South Africa). In the future, the current efforts of the IAEA to build a systematic database of available isotope measurements in rivers (IAEA, 2012) will allow for a more thorough evaluation of these model results.

To close the global water budget, the HD scheme not only simulates the water transport via large river systems, but also redistributes all net surplus water of terrestrial P–E fluxes to a nearby coastal grid point by following orographic gradients. The $\delta^{18}\text{O}$ values of the resulting annual mean water inflow of the coastal grid points to the ocean are shown in Fig. 5b.

4.1.4 Deuterium excess in meteoric and ocean surface waters

In Fig. 6 we show the simulated dex signal in evaporation, precipitation, and ocean surface waters. Dex values in the evaporation flux (Fig. 6a) range between -2 and $+16$ ‰. The lowest values are found in extreme cold and windy regions of the Arctic, parts of the North Atlantic, and above surface waters of the Antarctic Circumpolar Current (ACC). Further negative dex values are simulated for parts of the Sahara and the Arabian Peninsula, but these values occur in regions of extremely low evaporation fluxes from the terrestrial surface and are not meaningful, but represent numerical artefacts caused by the division of two small numerical values for calculating the $\delta^{18}\text{O}$ and δD values. Maximum dex values of up to $+14$ ‰ are detected in various regions of the Earth, both above terrestrial and marine surfaces. The model results show some agreement with the predicted dex values in evaporation by Pfahl and Sodemann (2014), but it is very difficult to further evaluate this simulated pattern of dex in the evaporation flux, as no systematic data collection of this quantity exists, so far. For precipitation (Fig. 6b), modelled dex_p values range between 0 and $+18$ ‰, with the highest values in northern parts of the Sahara and a band-like structure covering the mountain regions of Iraq, the Hindu Kush, and large parts of the Himalayan plateau. The lowest values occur in dry regions of the southern Sahara and the Arabian Peninsula, northern India, and northern Brazil. The Southern Ocean is another region with simulated low dex_p values. For the Antarctic continent, the large-scale dipole of low (high) dex values in West (East) Antarctica is well captured by the model. For ocean surface waters (Fig. 6d), the simulated variations in deuterium excess are an order of magnitude lower than in precipitation and range between -1.6 and $+1.6$ ‰. Model results reveal a clear distinction with rather low dex values in mid- to low-latitudinal Atlantic regions, the highest dex values in the Arctic Ocean and the Baltic Sea, and rather small variations (± 0.4 ‰) in the remaining oceans. Both positive and negative anomalies are directly linked to the hydrological balance in the particular regions: in the low- to mid-latitudinal Atlantic Ocean, a net freshwater export exists. As the evaporated and exported water masses have a positive dex composition, the remaining ocean surface waters will become negative in their dex composition due to mass balance. In contrast, a region like the Baltic Sea has a positive mass balance; that is, total P–E from the Baltic Sea (including its catchment area) is positive and the excess water masses flow via the Skagerrak into the Atlantic Ocean. The surplus of precipitation leads to the positive dex signal in the Baltic Sea. A similar feature is detected for the Arctic Ocean.

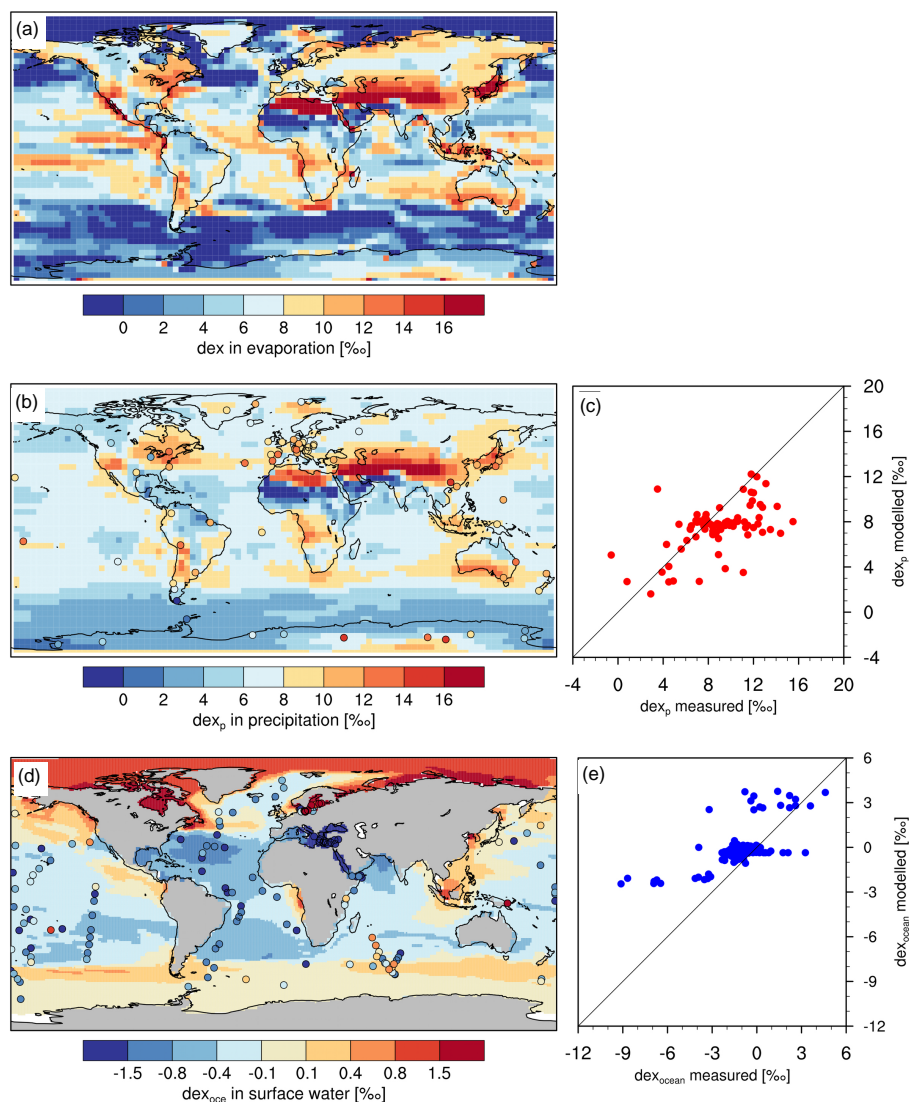


Figure 6. Global distribution of simulated and observed annual mean deuterium excess (dex) values in (a) evaporation, (b) precipitation, and (d) ocean surface waters. The background pattern shows the dex distribution as simulated by ECHAM5/MPI-OM. In panel (b), data from 70 GNIP stations and 21 ice cores from Greenland and Antarctica are plotted as coloured symbols. In panel (d), 153 data entries from the GISS database are plotted as coloured symbols. Comparison of observed present-day dex values in (c) precipitation (red symbols) and in (e) ocean surface waters (blue symbols) vs. the corresponding modelled dex values of the PI simulation. The black lines in panels (c) and (e) represent the 1 : 1 line indicating a perfect model fit.

To evaluate the simulated global distribution of dex in precipitation and ocean surface waters, we use again the GNIP and GISS data sets. The plotted station values in Fig. 6c, e do not show a systematic regional bias of the modelled dex signal in precipitation (Fig. 6c) or ocean surface waters (Fig. 6e). We note that some of the measured dex values, e.g. a series of GISS data points in the southern Indian Ocean, show strong small-scale variations that cannot be matched due to the coarse horizontal model resolution. However, even on a large-scale average, the model results tend to underestimate the dex values in precipitation, with a

RMSE of 2.9 ‰, while the simulated dex values of ocean surface waters are in general higher (RMSE: 1.8 ‰) than measurements listed in the GISS database. The modelled slope between the simulated dex in vapour above the ocean surface and the related relative humidity RH ($-6.3\text{‰}/(10\text{‰ RH change})$) is very close to the value given by Merlivat and Jouzel (1979) though. The combination of underestimation (overestimation) of simulated dex values in precipitation (ocean surface waters) might indicate that the general description of fractionation processes during the evaporation of ocean surface waters, implemented as proposed by Mer-

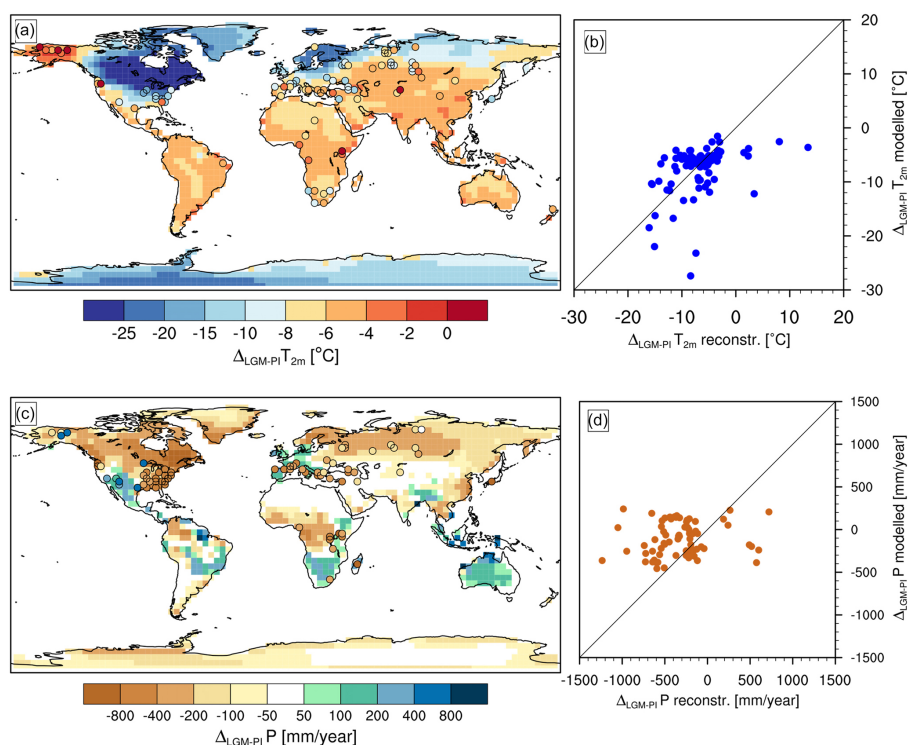


Figure 7. (a) Background pattern: simulated global pattern of annual mean surface temperature (T_{2m}) changes between the LGM and PI climate. Pollen-based reconstructed temperature changes by Bartlein et al. (2011) are shown as coloured symbols. (b) Comparison of reconstructed temperature changes shown in panel (a) vs. the simulated LGM-PI cooling at the sample locations. The black line represents the 1 : 1 line indicating a perfect model fit. (c) Simulated global pattern of annual mean precipitation changes between the LGM and PI climate. (d) Comparison of reconstructed precipitation changes shown in panel (b) vs. the simulated LGM-PI change at the sample locations. The black line represents the 1 : 1 line indicating a perfect model fit.

livat and Jouzel (1979), should be revised and refined. This finding is in agreement with recent studies by Steen-Larsen et al. (2014b, a, 2015), which reveal substantial deviations of the simulated dex signal in water vapour in Greenland, Bermuda, and Iceland, by several atmosphere GCMs as compared to laser-based spectroscopy measurements of isotopes in water vapour.

4.2 Changes in the Last Glacial Maximum

4.2.1 Land surface temperature and precipitation changes

Due to the prescribed changed glacial ice sheet configuration, changed orbital parameters, and changed greenhouse gas concentrations, the simulated LGM climate in glacier-free terrestrial areas is on average -5.9°C colder than the modelled PI climate. Most regions show a rather uniform cooling in the range of -4 to -8°C (Fig. 7a). Exceptionally cold regions are mostly adjacent to the prescribed Laurentide and Fennoscandian ice sheet, e.g. part of central North America and central Europe. Another region of exceptional cooling is a large part of Siberia, with a cooling of down to -15°C . The only region with a distinct above-average warming is lo-

cated in Alaska. This region most likely warmed during the LGM due to the increased distance to sea ice-covered Arctic Ocean regions, caused by the glacial sea-level drop of approx. 120 m. Our results are in overall agreement with the ensemble-mean LGM changes in temperature by the fully coupled climate simulations performed within the PMIP2 and CMIP5/PMIP3 projects (not shown; Braconnot et al., 2007; Harrison et al., 2014). These simulations also indicate for the LGM a maximum cooling of surface temperature over the ice sheets of about -30° and an average cooling of glacier-free land surfaces of between -2 and -5°C , except for a colder-than-average Siberian region.

For a comparison with proxy data, we compare our model results to the LGM continental temperature and precipitation reconstruction by Bartlein et al. (2011). This reconstruction is mainly based on subfossil pollen and plant macrofossil data. For the 81 sites contained in the temperature data set of Bartlein et al. (2011), the simulated annual mean LGM temperature change is in 24 cases (24 cases) more than 2°C warmer (colder) than the reconstructed temperature change (Fig. 7b). While the model–data deviations of LGM warming anomalies range between $+0$ and $+20^{\circ}\text{C}$, the anomalies of LGM cooling are underestimated by down to -15°C . Sev-

eral sites with the largest model–data deviations are located near the border of the prescribed Laurentide and Fennoscandian ice sheets. These deviations might simply be caused by the rather coarse model resolution of $3.8^\circ \times 3.8^\circ$, which cannot resolve small-scale temperature changes close to the prescribed glacier area in sufficient detail.

Simulated LGM precipitation changes (Fig. 7c) show a drying of large parts of Siberia and North America, and smaller parts of South America, Africa, and East Asia. A wetting is found for the region of California, western Europe, the Brazilian highlands, South Africa, and most parts of Australia. Especially the regions of a wetter LGM climate strongly deviate from older PMIP2 simulations (Brannan et al., 2007), but are in good overall agreement with the latest CMIP5 LGM experiments (Harrison et al., 2014). A comparison of the simulation results with the precipitation reconstruction by Bartlein et al. (2011) reveals less agreement between simulated and reconstructed precipitation (Fig. 7c, d). In agreement with the reconstructions, the model simulates a drying over vast parts of northern Eurasia and Siberia, as well as a dipole pattern of wetter (drier) conditions south of the margin of the Laurentide ice sheet in western (eastern) North America. However, the model fails to simulate a drying of western and central Europe during the LGM, as indicated by fossil plant data. Overall, the amplitude of modelled changes in the hydrological cycle (-460 to $+270 \text{ mm year}^{-1}$) is weaker than the range of the reconstructed changes (-1240 to $+720 \text{ mm year}^{-1}$), and the general underestimation of LGM dryness is in line with model results from the PMIP2 and CMIP5/PMIP3 projects (Harrison et al., 2014).

4.2.2 LGM changes in $\delta^{18}\text{O}$ in precipitation

Previous studies have already shown that the colder climate of the LGM leads to generally more depleted $\delta^{18}\text{O}_p$ values in precipitation (Lee et al., 2008; Risi et al., 2010a). This depletion is a direct consequence of the changed (temperature-dependent) fractionation strength during both evaporation and condensation processes. Over glacier-free land surfaces, we calculate a precipitation-weighted mean decrease in $\delta^{18}\text{O}_p$ in precipitation by -0.24‰ . For tropical and subtropical regions in Central and South America, Africa, Australia, and parts of Asia, our simulation reveals almost no LGM–PI changes in $\delta^{18}\text{O}_p$ in precipitation (Fig. 8a). Glacial changes of down to -3‰ occur in precipitation over the southern parts of South America and Africa, the Tibetan Plateau, as well as over major parts of Siberia, North America, and Alaska. The strongest simulated LGM–PI changes in $\delta^{18}\text{O}_p$ in precipitation (down to -12‰) are found over the glacier areas of both the Northern Hemisphere and Southern Hemisphere. We restrict a first quantitative evaluation of the simulated LGM–PI $\delta^{18}\text{O}_p$ anomalies in precipitation to the chosen data of 21 ice cores (Table 1) and 8 speleothem records (Table 2). Our data set is partly identical to the one

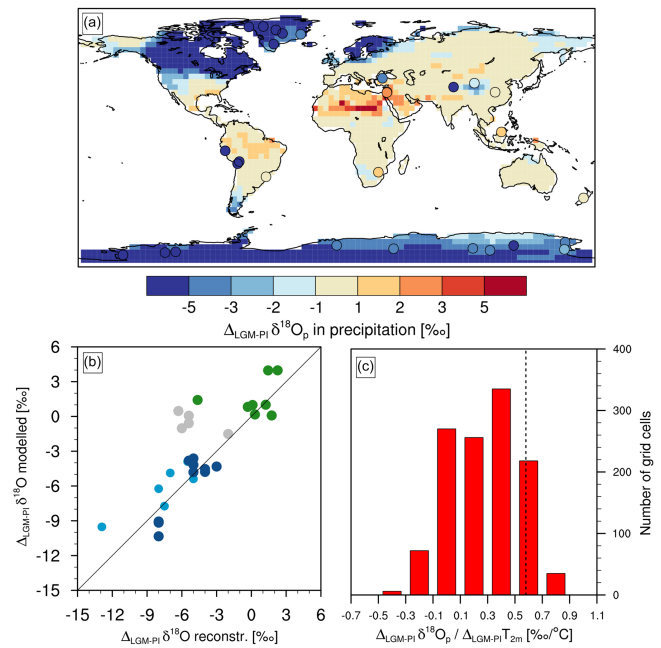


Figure 8. (a) Background pattern: simulated global pattern of annual mean $\delta^{18}\text{O}_p$ changes in precipitation between the LGM and PI climate. Reconstructed $\delta^{18}\text{O}_p$ in precipitation changes in ice cores (Table 1) and $\delta^{18}\text{O}_c$ in calcite of speleothems (Table 2) are shown as coloured symbols. (b) Comparison of reconstructed $\delta^{18}\text{O}$ changes shown in panel (a) vs. the simulated LGM–PI $\delta^{18}\text{O}$ changes at the same locations. Reconstructed $\delta^{18}\text{O}_p$ anomalies stem from the following archives: Antarctica (dark blue), Greenland (light blue), and tropical ice cores (grey). For speleothems, reconstructed and simulated $\delta^{18}\text{O}_c$ changes are shown (green). The black line represents the 1 : 1 line indicating a perfect model fit. (c) Histogram of calculated temporal LGM–PI $\delta^{18}\text{O}_p$ – T gradients for all grid cells with (i) an annual mean PI temperature below $+20^\circ\text{C}$ and (ii) a simulated LGM–PI cooling of at least -2° . The dashed line indicates the modelled PI spatial $\delta^{18}\text{O}_p$ – T gradient ($0.58\text{‰}/^\circ\text{C}$).

used by Risi et al. (2010a) and by Brennan et al. (2012) and enables a direct comparison with these previous model studies. For the ice core records, we compare the modelled change in $\delta^{18}\text{O}_p$ in precipitation with the ice core data (Table 1). For the speleothem records, we use both the simulated LGM–PI temperature and $\delta^{18}\text{O}_p$ changes to calculate the modelled change in $\delta^{18}\text{O}_c$ in calcite, which is then compared with the reconstructions (Table 2). Overall, the model results agree well ($r^2 = 0.64$, $\text{RMSE} = 2.7\text{‰}$) with the reconstructed LGM–PI $\delta^{18}\text{O}$ changes at the various sites (Fig. 8b). The largest deviations are found for the Camp Century ice core (measured LGM–PI $\delta^{18}\text{O}_p$ difference: -12.9‰ ; modelled: -9.5‰) and for the $\delta^{18}\text{O}_p$ in precipitation at four out of five tropical ice core locations.

From the simulated LGM–PI temperature and $\delta^{18}\text{O}_p$ changes we calculate the temporal $\delta^{18}\text{O}_p$ – T gradient m in a specific grid box as $m = (\delta^{18}\text{O}_{p,\text{LGM}} - \delta^{18}\text{O}_{p,\text{PI}}) / (T_{\text{LGM}} - T_{\text{PI}})$, with T as the surface temperature at the precipitation

site. We restrict our calculation to mid- and high-latitude regions with an annual mean PI temperature T_{PI} below +20 °C. As a further selection criterion, we use grid cells with a simulated LGM–PI cooling of at least −2 °C only. The calculated temporal $\delta^{18}O_p$ – T gradient m for the selected grid cells ($N = 1195$) ranges between −0.53 and +0.85 (Fig. 8c). For only 18 % of the grid cells ($N = 218$), the calculated temporal $\delta^{18}O_p$ – T gradient ranges between +0.5 and +0.7 ‰/°C, close to the simulated modern spatial $\delta^{18}O_p$ – T gradient of $m = 0.58$ ‰/°C (see Sect. 4.1.1). In the vast majority of the grid cells (79 %), the temporal $\delta^{18}O_p$ – T gradient is below the modern spatial one, while a higher temporal gradient is simulated for 3 % of the selected cells only. A clear difference between temporal and spatial $\delta^{18}O_p$ – T gradients has already been reported for Greenland (Buizert et al., 2014; Jouzel, 1999; Werner et al., 2000) and might be caused by different mechanisms (e.g. change in precipitation seasonality, shift of water vapour source regions and transport pathways, varying vertical temperature gradients and atmospheric heights of precipitation formation). However, our results indicate that such a potential bias of the $\delta^{18}O_p$ thermometer (if a modern spatial $\delta^{18}O_p$ – T gradient is used for past temperature reconstructions) might not exist for Greenland only, but also for large parts of the mid- and high-latitude regions. The robustness and implications of these findings will be further investigated in future studies.

Next, we take a more detailed look at the simulation results over both polar ice caps. For the extended compilation of ice core data listed in Table 1, our model results are in good agreement with glacial $\delta^{18}O_p$ anomalies found in Antarctic ice cores (Fig. 9). Mean model–data deviation is 1.1 ‰ with the largest mismatch for the Byrd ice core (2.5 ‰). For Greenland, model–data differences are slightly higher than for Antarctica, as the model underestimates the LGM–PI $\delta^{18}O_p$ changes by 1.6 ‰, on average. As already noted above, the largest mismatch is found for the Camp Century ice core (3.4 ‰). The reason for this stronger model–data mismatch for Greenland as compared to Antarctica could be partly due to the coarse model resolution, or caused by an erroneous warm bias of SST in the source regions of vapour transported to Greenland. Testing and evaluating these different hypotheses will require further coupled simulations and analyses.

4.2.3 LGM changes in ocean temperatures and marine $\delta^{18}O$ signals

The state of the glacial oceans has been under debate since the first reconstruction of global LGM sea surface temperatures (SSTs) and sea ice coverage by the CLIMAP group (CLIMAP Project Members, 1976). As compared to CLIMAP, the most recent SST reconstruction by the MARGO project (MARGO Project Members, 2009) indicates, among others, a more pronounced cooling in the eastern mid-latitude North Atlantic than in the western basin,

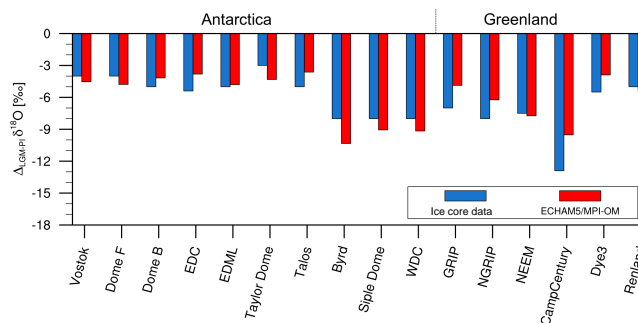


Figure 9. Comparison of annual mean LGM $\delta^{18}O_p$ anomalies measured in ice cores from Antarctica and Greenland (blue bars) vs. the simulated ECHAM5/MPI-OM LGM–PI $\delta^{18}O_p$ changes (red bars) at the ice core locations.

ice-free conditions in the Nordic seas during glacial summer, as well as a 1–3 °C cooling of the western Pacific warm pool. The study also revealed the presence of large longitudinal gradients in LGM SST anomalies in all the ocean basins, which are absent in the majority of atmosphere–ocean coupled simulations of the PMIP2 project (MARGO Project Members, 2009).

The physical state of the glacial ocean of our LGM simulation has already been analysed and described in detail by Zhang et al. (2013). In agreement with this previous study, we also find a rather uniform SST cooling in the range of 2–4 °C during the LGM in our simulation, comparable to the results of several atmosphere–ocean GCMs participating in PMIP2 and CMIP5/PMIP3 (Zhuang and Giardino, 2012). For the isotopic composition of ocean surface waters $\delta^{18}O_{oce}$, we simulate a globally averaged mean increase of +0.84 ‰ as compared to the PI ocean state. This is noteworthy, as we adjusted in our LGM simulation the global ocean isotopic composition by +1 ‰ to account for the change in global ice volume. A less-than-average part of this increase (0.94 ‰) is found in surface and shallow water depth down to approx. 1000 m, while deeper water masses show a glacial increase of up to +1.06 ‰ in our simulation. In addition, the simulated glacial increase is not spatially uniform for the ocean surface waters either. For most regions the LGM anomalies are of the order of +0.5 to +1 ‰ (Fig. 10a), but more positive LGM $\delta^{18}O_{oce}$ anomalies exist in the ACC region (up to +1.5 ‰), the Mediterranean region (up to +3 ‰), as well as in the North Atlantic region above approx. 30° N (up to +2.3 ‰).

As both water temperatures and $\delta^{18}O_{oce}$ are explicitly simulated by our model set-up, we can calculate $\delta^{18}O_c(PDB)$ for the PI and LGM simulation and then compare our model results to the marine calcite $\delta^{18}O_c$ data set documented by Caley et al. (2014b). In agreement with the simulated pattern of LGM $\delta^{18}O_{oce}$ anomalies in seawater, the simulated $\delta^{18}O_c$ changes in calcite are strongest in the ACC region, the Mediterranean Sea and the North Atlantic. Positive

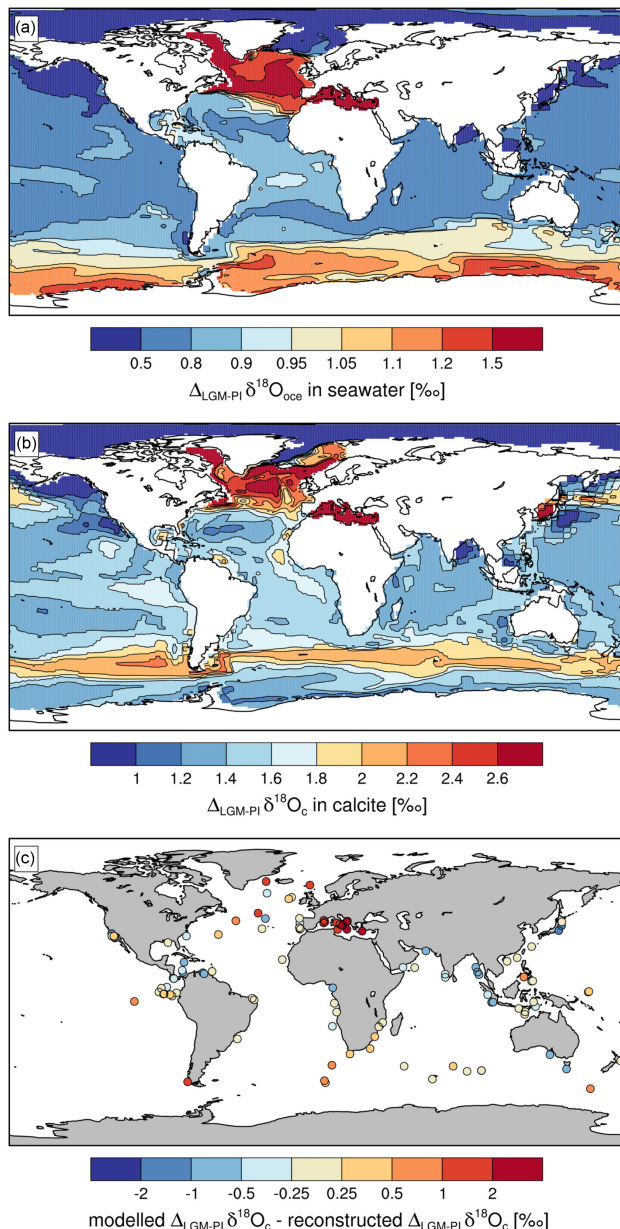


Figure 10. (a) Simulated global pattern of annual mean $\delta^{18}\text{O}_{\text{oce}}$ changes in ocean surface waters (0–50 m depth) between the LGM and PI climate. (b) Calculated global pattern of annual mean $\delta^{18}\text{O}_c$ changes in calcite in ocean surface waters between the LGM and PI climate. The $\delta^{18}\text{O}_c$ values are derived from the simulated $\delta^{18}\text{O}_{\text{oce}}$ changes shown in panel (a) and the modelled LGM–PI ocean temperature changes (see text for details). (c) Difference between simulated LGM–PI $\delta^{18}\text{O}_c$ changes and LGM–Late Holocene $\delta^{18}\text{O}_c$ anomalies of a compilation of 114 planktic foraminifera data entries compiled by Caley et al. (2014b).

$\delta^{18}\text{O}_c$ anomalies reach maximum values of +2.6 ‰ in the North Atlantic. Comparing the pattern of simulated LGM–PI changes in $\delta^{18}\text{O}_{\text{oce}}$ in surface waters (Fig. 10a) and $\delta^{18}\text{O}_c$ in calcite (Fig. 10b), it is also noteworthy that (a) there exists

an additional strong positive LGM $\delta^{18}\text{O}_c$ anomaly in the East China Sea and parts of the North Pacific, which has no counterpart in the $\delta^{18}\text{O}_{\text{oce}}$ changes in ocean surface waters, and that (b) the $\delta^{18}\text{O}_c$ anomalies in the Pacific ACC region are shifted northwards by approx. 5° as compared to the $\delta^{18}\text{O}_{\text{oce}}$ surface water anomalies.

A comparison of the simulated $\delta^{18}\text{O}_c$ values in ocean surface waters between 0 and 50 m to the $\delta^{18}\text{O}_c$ data set of planktic LGM $\delta^{18}\text{O}_c$ anomalies compiled by Caley et al. (2014b) shows a systematic overestimation of simulated LGM $\delta^{18}\text{O}_c$ changes for the Mediterranean Sea (Fig. 10c). For all three major oceans, our model simulation both underestimates and overestimates LGM $\delta^{18}\text{O}_c$ changes at various marine sediment sites. Model–data differences are mostly within the order of the reported uncertainty of the reconstructed LGM $\delta^{18}\text{O}_c$ anomalies, as reported by Caley et al. (2014b). The simulated spatial pattern of LGM $\delta^{18}\text{O}_c$ anomalies in surface waters shows some remarkable resemblance to the model results of Caley et al. (2014b) using the iLOVECLIM model. In their study, Caley et al. also find the strongest positive $\delta^{18}\text{O}_c$ anomalies in the North Atlantic, parts of the northern Pacific, as well as in the ACC. In contrast to our simulation, Caley et al. report an additional strong $\delta^{18}\text{O}_c$ anomaly in the northern Indian Ocean.

In Fig. 11 mean LGM–PI changes in $\delta^{18}\text{O}_c$ for the Atlantic cross section ($60^\circ\text{--}0^\circ\text{W}$) and the Pacific cross section (150°E to 110°W) are shown. For both oceans, model results show the strongest positive change in $\delta^{18}\text{O}_c$ between 500 and 3000 m. While $\delta^{18}\text{O}_c$ changes of up to +2.6 ‰ are simulated at around 30°N for the Atlantic basin, the $\delta^{18}\text{O}_c$ changes in the Pacific water masses are in general lower (up to +2.2 ‰), and the region of the largest change is located between 0 and 50°S . The available benthic foraminifera data compiled by Caley et al. (2014b) partly support these findings. The overly positive modelled $\delta^{18}\text{O}_c$ values in the North Atlantic at depths between approx. 2500 and 4000 m indicate that the simulated NADW formation is probably too strong and too deep. By combining a series of isotope studies with different NADW strengths with available proxy studies of the glacial NADW formation (Duplessy et al., 1980), it should be possible to constrain and improve this aspect of the isotope-enhanced version of the ECHAM5/MPI-OM model. Recently, Roche et al. (2014) presented a similar approach for an improved modelling of Heinrich event 1. However, performing such a set of fully coupled sensitivity experiments is computationally demanding and beyond the scope of this paper.

4.2.4 Glacial changes in the deuterium excess

In Fig. 12a, we show the global pattern of simulated LGM–PI dex anomalies in precipitation over land surfaces. Changes are rather minor, of the order of -3 to $+3$ ‰, except for a clear positive anomaly (up to +6 ‰) in North America southwest of the Laurentide ice sheet margin, and strong negative

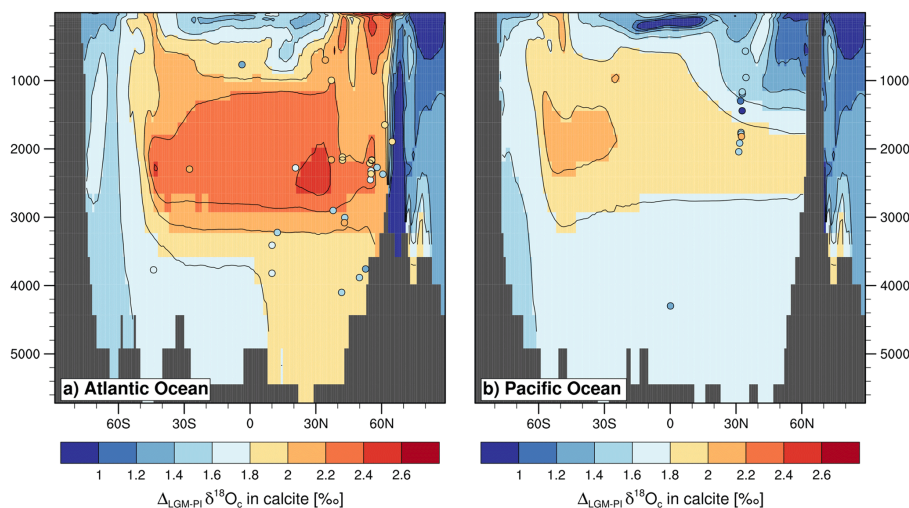


Figure 11. Background pattern: meridional section of the simulated annual mean LGM-PI $\delta^{18}\text{O}_c$ in calcite changes in (a) the Atlantic (zonal mean over 60 to 0° W) and (b) the Pacific (zonal mean over 150° E to 110° W). Geographically related data entries from a compilation of 115 LGM–Late Holocene $\delta^{18}\text{O}_c$ anomalies of benthic foraminifera data compiled by Caley et al. (2014b) are plotted as coloured symbols (Atlantic Ocean: $n = 29$; Pacific Ocean: $n = 12$) in each panel.

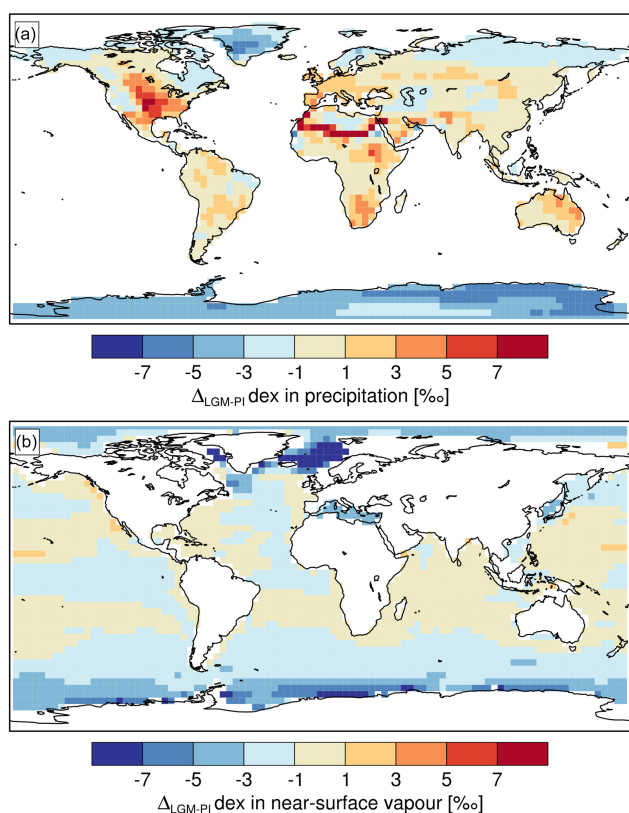


Figure 12. Global distribution of simulated annual mean LGM-PI deuterium excess (dex) changes in (a) continental precipitation and (b) water vapour of the lowest atmospheric model layer above the ocean surface.

anomalies (down to -7‰) above Greenland and Antarctica. For ocean surface waters, the simulated dex anomalies are even smaller and almost everywhere in the range of $\pm 1\text{‰}$ (not shown). Figure 12b shows the simulated LGM-PI dex anomalies in water vapour of the lowest atmospheric model layer above the ocean surface (discussed below).

As stated in Sect. 2, we assumed no glacial change in the mean deuterium excess signal in the glacial ocean. However, some recent data (Schrag et al., 2002) suggest a mean glacial dD increase of $+7.2\text{‰}$, which is slightly lower than the increase prescribed in our LGM simulation ($+8\text{‰}$). Such a lower glacial dD increase would lead to a mean glacial change in the deuterium excess in ocean waters of -0.8‰ . As a first-order estimate, such a lowered deuterium excess signal in the ocean might lead to an equivalent lower deuterium excess value both in vapour above the ocean and, consequently, in precipitation.

So far, ice cores are the only paleoproxy archive, which allow for reconstructing past changes in deuterium excess values in precipitation. In Fig. 13 we compare our model results of annual mean dex changes in precipitation between the LGM and PI simulation with the compiled ice core data (Table 1). The mean absolute deviation between modelled LGM-PI anomalies and ice core data from Antarctica is 1.6‰ . For Greenland ice cores, LGM dex values have been only reported for the GRIP ice core so far. Here, model results underestimate the LGM-PI dex change by 2‰ . The overall good agreement between measured and modelled LGM dex changes is remarkable, as isotope-enabled GCMs have had some difficulties simulating the measured LGM dex changes in Antarctic ice cores so far (e.g. Risi et al., 2010a; Werner et al., 2001). As dex values in po-

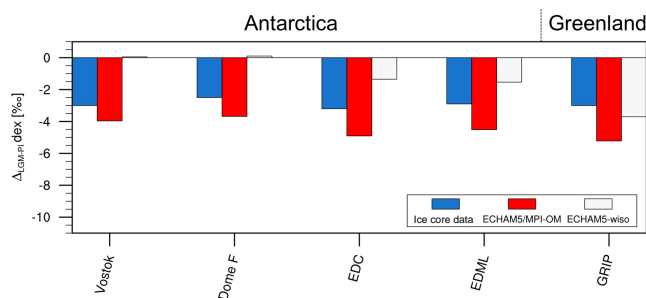


Figure 13. Comparison of annual mean LGM dex anomalies measured in ice cores from Antarctica and Greenland (blue bars) vs. simulated LGM-PI dex changes (ECHAM5/MPI-OM: red bars; ECHAM5-wiso: light grey bars) at the ice core locations.

lar ice cores depend on climate conditions during evaporation of the source water, and as the SSTs of our simulation are more uniform and lower than the latest MARGO reconstruction, one may ask whether the good dex agreement is due to the modelled SST. To test this hypothesis, we have conducted an atmosphere-only ECHAM5-wiso simulation with identical LGM boundary conditions as for the fully coupled ECHAM5/MPI-OM set-up but using the GLAMAP LGM SST reconstruction, which was supplemented by older CLIMAP data in order to have global coverage (Schäfer-Neth and Paul, 2003a, b). For $\delta^{18}\text{O}_{\text{Oce}}$ ($\delta\text{D}_{\text{Oce}}$), we prescribed a uniform glacial increase of $+1\text{‰}$ ($+8\text{‰}$) in this simulation. In this ECHAM5-wiso sensitivity study, the relatively warm (sub)tropical GLAMAP SST reconstruction leads to smaller simulated negative dex anomalies, or even slightly positive dex anomalies for Vostok and Dome F (Fig. 13). The RMSE of all Antarctic ice cores is 2.3‰ , which is 0.7‰ worse than in the fully coupled simulation. We are aware that such a comparison of the fully coupled ECHAM5/MPI-OM set-up with an atmosphere-only ECHAM5 experiment with prescribed SST might be hampered by neglecting any atmosphere–ocean feedback in the latter. Nevertheless, our simulations indicate that glacial SSTs, which are cooler than the GLAMAP reconstruction, lead to an improved simulation of dex changes, at least over Antarctica. However, for Greenland the simulated dex anomaly at the GRIP drilling site becomes too low in our fully coupled simulation. But as no more LGM-PI dex records of Greenland ice core records have been published, yet, it remains an open question whether this deviation points to a systematic bias in our simulation. More LGM-PI dex data from polar ice cores in combination with further isotope simulations are required to put an additional, highly valuable constraint on available LGM SST reconstructions.

Apart from glacial SST changes, changes in the source areas of water transported to Antarctica and Greenland, e.g. by a glacial change in sea ice coverage, might lead to the change in the deuterium excess signal in polar precipitation, too. The simulated sea ice coverage of the ECHAM5/MPI-

OM LGM simulation has already been described in detail in Zhang et al. (2013), and our simulation results are comparable to this previous study. For the Southern Hemisphere, there is a reasonable agreement between the simulated sea ice concentration and proxy data by Gersonde et al. (2005), such as the austral winter sea ice extent in the Atlantic sector and the austral summer sea ice extent in the Indian Ocean sector. However, the simulation might underestimate a larger extent of sporadic summer sea ice between 5°E and 5°W in the Southern Ocean, as discussed in Gersonde et al. (2005). As compared to the ECHAM5 experiment with GLAMAP data, a much-reduced sea ice cover in austral summer is found in this coupled ECHAM5/MPI-ESM LGM simulation. This reduction might lead to a stronger contribution of vapour stemming from regions between 60 and 65°S to the Antarctic ice sheet. As vapour from these regions has a strong negative deuterium excess signal (cf. Fig. 12), such a shift in the source contributions might lead to a more negative deuterium excess signal in Antarctic precipitation too.

Pfahl and Soedemann (2014) suggest in their study that the typical interpretation of dex variations in ice core records as SST changes might have to be adapted to reflect climatic influences on relative humidity during evaporation. To test this hypothesis, we look at the simulated LGM-PI dex anomalies in water vapour of the lowest atmospheric layer, directly above the ocean surface (Fig. 12b). It is safe to assume that most water transported to Antarctica will stem from Southern Hemisphere marine vapour source regions, and not from continental vapour sources. Simulated LGM-PI dex anomalies of the vapour vary between 0 and -5‰ for most ocean regions, with a clear gradient towards more negative dex values in the higher latitudinal regions. Plotting these simulated changes in dex in vapour against the modelled relative humidity change between LGM and PI over the ocean surface reveals no correlation between these humidity changes and the simulated dex variations in the vapour layer. As seen in Fig. 14a, simulated LGM values of the relative humidity of the vapour layer above the ocean surface vary just by $\pm 5\%$ as compared to the PI values. These rather small variations of the LGM relative humidity changes are somewhat surprising, as cooler SSTs should lead to cooler air temperatures above the ocean surface, which then should lead to higher relative humidity levels (if the amount of water in the air stays constant). However, we find in our simulations that the air directly above the ocean surface cools slightly more during the LGM than the SSTs themselves. This leads to a reduced glacial evaporation flux from the ocean to the atmosphere, which decreases the relative humidity of the vapour and counterbalances the first effect. Similar small changes in relative humidity above the ocean surface and the counterbalance of different effects have recently been reported for a set of CMIP5 climate model results by Lañé et al. (2014). They have analysed a future warmer climate, though. In contrast, modelled LGM SST changes in the Southern Hemisphere cover a range of 0 to -15°C , and a strong corre-

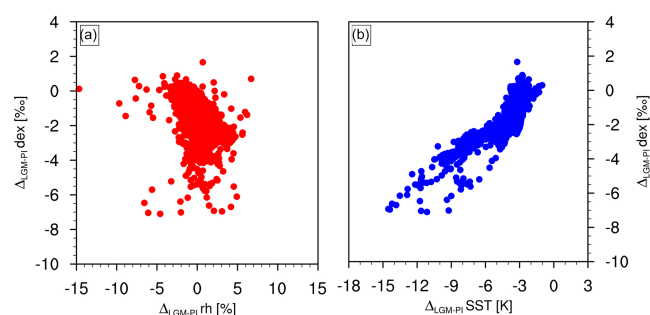


Figure 14. Relation between simulated LGM-PI deuterium excess (dex) changes in Southern Hemisphere water vapour of the lowest atmospheric model layer above the ocean surface vs. simulated LGM-PI changes in (a) relative humidity above the Southern Hemisphere ocean surface (RH, red symbols); (b) Southern Hemisphere sea surface temperatures (SSTs, blue symbols).

lation ($r^2 = 0.78$) between simulated glacial SST changes and LGM dex anomalies in the vapour above the ocean surface is found (Fig. 14b). We rate this finding as a support of the “classical” interpretation of dex changes in Antarctic ice cores as a proxy for SST changes in the source regions of water transported to Antarctica. However, the correlation between vapour dex and SST changes does not rule out other influencing factors, like wind speed changes, which might affect both the deuterium excess signal and SST changes, simultaneously. Furthermore, we are aware that several recent studies of dex in water vapour have revealed a large bias between measurements and simulations by different isotope-enabled atmospheric GCMs (Steen-Larsen et al., 2014b, 2015). We cannot resolve this conundrum with the performed simulations and will investigate this topic in more detail in the future.

5 Summary and conclusions

In this study we present the first simulations of the fully coupled ECHAM5/MPI-OM Earth system model. The model has been enhanced by an explicit stable water isotope diagnostics in all relevant model components: atmosphere, land surface, terrestrial discharge, and ocean. The hydrological cycle and its isotopic balance are fully closed in the model set-up, and the model has been run successfully into equilibrium under PI and LGM boundary conditions.

First-order isotope variations in precipitation ($\delta^{18}\text{O}_p$, δD_p) for the PI and LGM climate are in good to very good agreement with available present-day observations from the GNIP database, and with LGM isotope data from various ice core and speleothem records. The largest δ deviations between present-day observations and model results are found in high-latitude regions and are caused by a warm bias of the coupled model, similar to the reported error of the ECHAM5-wiso atmosphere-only GCM (Werner et al., 2011). Such a

warm bias, especially over Antarctica, is frequent in GCMs (Masson-Delmotte et al., 2006) and is partly related to the coarse spatial resolution of our model set-up.

The simulated modern spatial δ – T relation is also in good agreement with the observed one, based on a selection of GNIP and ice core data. A first assessment of the stability of this relation for LGM-PI climate changes reveals that the temporal δ – T gradient might have been substantially lower than the modern spatial one for most mid- to high-latitude regions. Such a deviation, which causes a strong bias in the “classical” δ -paleothermometry approach, is known for Greenland ice cores (Jouzel, 1999), but has not been discussed for other Northern Hemisphere regions so far. Future in-depth analyses of our model results can help to achieve an improved interpretation of available isotope records, e.g. from speleothems or permafrost ice wedges (Meyer et al., 2015), from these regions.

For the PI climate, simulated marine $\delta^{18}\text{O}_{\text{oce}}$ values broadly fit to available measurements compiled in the GISS database. For the Atlantic, Pacific, and Indian oceans, the largest model–data deviations in ocean surface waters are found in the vicinity of large river estuaries, the Sea of Okhotsk, parts of the Bering Sea, and the Baltic Sea. Like for the model deficits in $\delta^{18}\text{O}_p$, these deviations are most likely related to the rather coarse resolution of the MPI-OM ocean model component, which hampers a realistic simulation of water mass mixing in these coastal regions. For the Arctic, modelled $\delta^{18}\text{O}_{\text{oce}}$ values in surface waters show a more general negative bias as compared to the GISS data. It remains an open question whether this bias can also be simply related to an inadequate mixing of the isotopically depleted inflow of Arctic rivers into this ocean basin, or whether a more general model bias in the hydrological balance of the Arctic Ocean exists. For the simulated LGM $\delta^{18}\text{O}$ changes, a comparison of model results with available $\delta^{18}\text{O}_c$ calcite data from planktic and benthic foraminifera shells reveals a partial model–data match only. For the North Atlantic, the modelled glacial NADW formation appears too deep and too strong in our LGM simulation. However, more sensitivity studies are necessary to better constrain this aspect of glacial ocean circulation change. As a next step, we will also more explicitly simulate the dependence of $\delta^{18}\text{O}_c$ on the surrounding water conditions, and analyse the stability of the relation between $\delta^{18}\text{O}$ and salinity in ocean waters under the different climate conditions.

The simulation results for second-order changes in $\delta^{18}\text{O}$ and δD are also satisfactory. In our analyses, an overall good fit of modern deuterium excess values in precipitation and ocean surface waters with the available observations is found. However, on large-scale average, the ECHAM5/MPI-OM isotope results tend to slightly underestimate the dex values in precipitation and, at the same time, overestimate the simulated dex values of ocean surface waters. This combination of opposite biases suggests that the implementation of fractionation processes during the evaporation of ocean surface wa-

ters in our model set-up, which strictly follows the approach by Merlivat and Jouzel (1979), should maybe be revised and refined in future studies. For LGM-PI changes in deuterium excess, only measurements from Greenland and Antarctic ice cores are available at present. Our simulation results indicate that LGM Southern Hemisphere SSTs, which are cooler than the MARGO reconstruction, lead to an improved simulation of dex values in Antarctic precipitation. In addition, our analyses reveal that modelled glacial dex changes are strongly correlated with LGM-PI SST changes, but not with relative humidity changes in the evaporation regions.

In this study we have presented the first results of the newly developed isotope-enabled version of the ECHAM5/MPI-OM Earth system model. We have focused on two equilibrium simulations under the pre-industrial and Last Glacial Maximum period, only, due to their different climate states and the wealth of available observational data from both periods. Future studies will investigate changes in the hydrological cycle and its isotopic composition for further climate periods of the past, e.g. the last interglacial, as well as for the transition between them.

Acknowledgements. The work of B. Haese was funded by Deutsche Forschungsgemeinschaft (DFG) as part of the project HYDRACENE (A new hydrogen-isotope approach to understand north African monsoon changes in the Holocene) within the framework of the Special Priority Programme INTERDYNAMIK. The work of M. Butzin was supported by a grant from the Russian government under the contract 11.G34.31.0064. We also thank three anonymous referees for their work and constructive comments to improve the manuscript.

Edited by: D. Roche

References

- Baertschi, P.: Absolute ¹⁸O content of standard mean ocean water, *Earth Planet. Sc. Lett.*, 31, 341–344, doi:10.1016/0012-821X(76)90115-1, 1976.
- Bartlein, P. J., Harrison, S. P., Brewer, S., Connor, S., Davis, B. A. S., Gajewski, K., Guiot, J., Harrison-Prentice, T. I., Henderson, A., Peyron, O., Prentice, I. C., Scholze, M., Seppä, H., Shuman, B., Sugita, S., Thompson, R. S., Viau, A. E., Williams, J., and Wu, H.: Pollen-based continental climate reconstructions at 6 and 21 ka: a global synthesis, *Clim. Dynam.*, 37, 775–802, doi:10.1007/s00382-010-0904-1, 2011.
- Bigg, G. R. and Rohling, E. J.: An oxygen isotope data set for marine waters, *J. Geophys. Res.-Oceans*, 105, 8527–8535, 2000.
- Bonne, J.-L., Masson-Delmotte, V., Cattani, O., Delmotte, M., Risi, C., Sodemann, H., and Steen-Larsen, H. C.: The isotopic composition of water vapour and precipitation in Ivittuut, southern Greenland, *Atmos. Chem. Phys.*, 14, 4419–4439, doi:10.5194/acp-14-4419-2014-supplement, 2014.
- Braconnot, P., Otto-Bliesner, B., Harrison, S., Joussaume, S., Peterchmitt, J.-Y., Abe-Ouchi, A., Crucifix, M., Driesschaert, E., Fichefet, Th., Hewitt, C. D., Kageyama, M., Kitoh, A., Laîné, A., Loutre, M.-F., Marti, O., Merkel, U., Ramstein, G., Valdes, P., Weber, S. L., Yu, Y., and Zhao, Y.: Results of PMIP2 coupled simulations of the Mid-Holocene and Last Glacial Maximum – Part 1: experiments and large-scale features, *Clim. Past*, 3, 261–277, doi:10.5194/cp-3-261-2007, 2007.
- Brennan, C. E., Weaver, A. J., Eby, M., and Meissner, K. J.: Modelling oxygen isotopes in the University of Victoria Earth System Climate Model for pre-industrial and last glacial maximum conditions, *Atmos. Ocean*, 50, 447–465, doi:10.1080/07055900.2012.707611, 2012.
- Broecker, W. S., Peng, T. H., Jouzel, J., and Russell, G.: The magnitude of global fresh-water transports of importance to ocean circulation, *Clim. Dynam.*, 4, 73–79, doi:10.1007/BF00208902, 1990.
- Brovkin, V., Raddatz, T., Reick, C. H., Claussen, M., and Gayler, V.: Global biogeophysical interactions between forest and climate, *Geophys. Res. Lett.*, 36, L07405, doi:10.1029/2009gl037543, 2009.
- Buizert, C., Gkinis, V., Severinghaus, J. P., He, F., Lecavalier, B. S., Kindler, P., Leuenberger, M., Carlson, A. E., Vinther, B., Masson-Delmotte, V., White, J. W. C., Liu, Z., Otto-Bliesner, B., and Brook, E. J.: Greenland temperature response to climate forcing during the last deglaciation, *Science*, 345, 1177–1180, 2014.
- Caley, T., Roche, D. M., and Renssen, H.: Orbital Asian summer monsoon dynamics revealed using an isotope-enabled global climate model, *Nature Communications*, 5, 377–380, doi:10.1038/ncomms6371, 2014a.
- Caley, T., Roche, D. M., Waelbroeck, C., and Michel, E.: Oxygen stable isotopes during the Last Glacial Maximum climate: perspectives from data-model (iLOVECLIM) comparison, *Clim. Past*, 10, 1939–1955, doi:10.5194/cp-10-1939-2014, 2014b.
- CLIMAP Project Members: Surface of Ice-Age Earth, *Science*, 191, 1131–1137, 1976.
- Coplen, T. B., Kendall, C., and Hopple, J.: Comparison of stable isotope reference samples, *Nature*, 302, 236–238, 1983.
- Craig, H. and Gordon, L. I.: Deuterium and oxygen 18 variations in the ocean and the marine atmosphere, edited by: Tongiogi, E., Consiglio nazionale delle ricerche, Laboratorio de geologia nucleare, Spoleto, Italy, 9–130, 1965.
- Cruz, F. W., Burns, S. J., Karmann, I., Sharp, W. D., Vuille, M., Cardoso, A. O., Ferrari, J. A., Dias, P. L. S., and Viana, O.: Insolation-driven changes in atmospheric circulation over the past 116 000 years in subtropical Brazil, *Nature*, 434, 63–66, doi:10.1038/Nature03365, 2005.
- Dansgaard, W.: Stable isotopes in precipitation, *Tellus*, 16, 436–468, 1964.
- Dansgaard, W., Johnsen, S. J., Møller, J., and Langway, C. C.: Oxygen isotope record for the Camp Century Greenland ice core, *Science*, 166, 377–380, 1969.
- Dayem, K. E., Molnar, P., Battisti, D. S., and Roe, G. H.: Lessons learned from oxygen isotopes in modern precipitation applied to interpretation of speleothem records of paleoclimate from eastern Asia, *Earth Planet. Sc. Lett.*, 295, 219–230, doi:10.1016/j.epsl.2010.04.003, 2010.
- Dee, D. P., Uppala, S. M., Simmons, A. J., Berrisford, P., Poli, P., Kobayashi, S., Andrae, U., Balmaseda, M. A., Balsamo, G., Bauer, P., Bechtold, P., Beljaars, A. C. M., van de Berg, L., Bid-

- lot, J., Bormann, N., Delsol, C., Dragani, R., Fuentes, M., Geer, A. J., Haimberger, L., Healy, S. B., Hersbach, H., Holm, E. V., Isaksen, I., Kallberg, P., Kohler, M., Matricardi, M., McNally, A. P., Monge-Sanz, B. M., Morcrette, J. J., Park, B. K., Peubey, C., de Rosnay, P., Tavolato, C., Thepaut, J. N., and Vitart, F.: The ERA-Interim reanalysis: configuration and performance of the data assimilation system, *Q. J. Roy. Meteor. Soc.*, 137, 553–597, doi:10.1002/Qj.828, 2011.
- Delaygue, G., Jouzel, J., and Dutay, J. C.: Oxygen 18–salinity relationship simulated by an oceanic general circulation model, *Earth Planet. Sc. Lett.*, 178, 113–123, doi:10.1016/S0012-821X(00)00073-X, 2000.
- de Wit, J. C., van der Straaten, C. M., and Mook, W. G.: Determination of the absolute hydrogen isotopic ratio of V-SMOW and SLAP, *Geostandards Newslett.*, 4, 33–36, doi:10.1111/j.1751-908X.1980.tb00270.x, 1980.
- Dodd, P. A., Rabe, B., Hansen, E., Falck, E., Mackensen, A., Rohling, E., Stedmon, C., and Kristiansen, S.: The freshwater composition of the Fram Strait outflow derived from a decade of tracer measurements, *J. Geophys. Res.*, 117, C11005, doi:10.1029/2012JC00801, 2012.
- Dreybrodt, W. and Scholz, D.: Climatic dependence of stable carbon and oxygen isotope signals recorded in speleothems: From soil water to speleothem calcite, *Geochim. Cosmochim. Ac.*, 75, 734–752, doi:10.1016/j.gca.2010.11.002, 2011.
- Duplessy, J. C., Moyes, J., and Pujol, C.: Deep-water formation in the North-Atlantic Ocean during the last Ice-Age, *Nature*, 286, 479–482, 1980.
- Fleitmann, D., Burns, S. J., Mudelsee, M., Neff, U., Kramers, J., Mangini, A., and Matter, A.: Holocene Forcing of the Indian Monsoon Recorded in a Stalagmite from Southern Oman, *Science*, 300, 1737–1739, doi:10.1126/science.1083130, 2003.
- Gersonde, R., Crosta, X., Abelman, A., and Armand, L.: Sea-surface temperature and sea ice distribution of the Southern Ocean at the EPILOG Last Glacial Maximum – A circum-Antarctic view based on siliceous microfossil records, *Quaternary Sci. Rev.*, 24, 869–896, doi:10.1016/j.quascirev.2004.07.015, 2005.
- Haese, B., Werner, M., and Lohmann, G.: Stable water isotopes in the coupled atmosphere–land surface model ECHAM5-JSBACH, *Geosci. Model Dev.*, 6, 1463–1480, doi:10.5194/gmd-6-1463-2013, 2013.
- Hagemann, S. and Gates, L. D.: Improving a subgrid runoff parameterization scheme for climate models by the use of high resolution data derived from satellite observations, *Clim. Dynam.*, 21, 349–359, doi:10.1007/s00382-003-0349-x, 2003.
- Harrison, S. P., Bartlein, P. J., Brewer, S., Prentice, I. C., Boyd, M., Hessler, I., Holmgren, K., Izumi, K., and Willis, K.: Climate model benchmarking with glacial and mid-Holocene climates, *Clim. Dynam.*, 43, 671–688, doi:10.1007/s00382-013-1922-6, 2014.
- Hibler, W. D.: A dynamic thermodynamic sea ice model, *J. Phys. Oceanogr.*, 9, 815–846, 1979.
- Hoffmann, G., Werner, M., and Heimann, M.: Water isotope module of the ECHAM atmospheric general circulation model: A study on timescales from days to several years, *J. Geophys. Res.-Atmos.*, 103, 16871–16896, 1998.
- Hoffmann, G., Ramirez, E., Taupin, J. D., Francou, B., Ribstein, P., Delmas, R., Durr, H., Gallaire, R., Simoes, J., Schotterer, U., Stiévenard, M., and Werner, M.: Coherent isotope history of Andean ice cores over the last century, *Geophys. Res. Lett.*, 30, 1179, doi:10.1029/2002gl014870, 2003.
- Hut, G.: Stable Isotope Reference Samples for Geochemical and Hydrological Investigations. Consultant Group Meeting IAEA, Vienna, 16–18 September 1985, Report to the Director General, International Atomic Energy Agency, Vienna, Austria, 1987.
- IAEA: Global Network of Isotopes in Rivers, available at: http://www-naweb.iaea.org/napc/ih/IHS_resources_gnir.html (last access: 15 May 2015), 2012.
- IAEA/WMO: Global Network of Isotopes in Precipitation: The GNIP Database, available at: <http://www.iaea.org/water> (last access: 15 May 2015), 2010.
- Johnsen, S. J., Dansgaard, W., Clausen, H. B., and Langway, C. C.: Oxygen isotope profiles through the Antarctic and Greenland ice sheets, *Nature*, 235, 429–434, 1972.
- Johnsen, S. J., Dahl-Jensen, D., Gundestrup, N., Steffensen, J. P., Clausen, H. B., Miller, H., Masson-Delmotte, V., Sveinbjornsdottir, A. E., and White, J.: Oxygen isotope and palaeotemperature records from six Greenland ice-core stations: Camp Century, Dye-3, GRIP, GISP2, Renland and NorthGRIP, *J. Quaternary Sci.*, 16, 299–307, 2001.
- Joussaume, S., Sadourny, R., and Jouzel, J.: A general circulation model of water isotope cycles in the atmosphere, *Nature*, 311, 24–29, 1984.
- Jouzel, J.: Calibrating the isotopic paleothermometer, *Science*, 286, 910–911, 1999.
- Jouzel, J.: A brief history of ice core science over the last 50 yr, *Clim. Past*, 9, 2525–2547, doi:10.5194/cp-9-2525-2013, 2013.
- Jouzel, J. and Merlivat, L.: Deuterium and oxygen 18 in precipitation: modeling of the isotopic effects during snow formation, *J. Geophys. Res.*, 89, 11749–11757, 1984.
- Jouzel, J., Russell, G. L., Suozzo, R. J., Koster, R. D., White, J. W. C., and Broecker, W. S.: Simulations of the HDO and H₂¹⁸O atmospheric cycles using the NASA GISS general circulation model: the seasonal cycle for present-day conditions, *J. Geophys. Res.*, 92, 14739–14760, 1987.
- Jouzel, J., Hoffmann, G., Koster, R. D., and Masson, V.: Water isotopes in precipitation: data/model comparison for present-day and past climates, *Quaternary Sci. Rev.*, 19, 363–379, 2000.
- Jouzel, J., Masson-Delmotte, V., Cattani, O., Dreyfus, G., Falourd, S., Hoffmann, G., Minster, B., Nouet, J., Barnola, J. M., Chappellaz, J., Fischer, H., Gallet, J. C., Johnsen, S., Leuenberger, M., Loulergue, L., Luethi, D., Oerter, H., Parrenin, F., Raisbeck, G., Raynaud, D., Schilt, A., Schwander, J., Selmo, E., Souchez, R., Spahni, R., Stauffer, B., Steffensen, J. P., Stenni, B., Stocker, T. F., Tison, J. L., Werner, M., and Wolff, E. W.: Orbital and millennial Antarctic climate variability over the past 800 000 years, *Science*, 317, 793–796, doi:10.1126/science.1141038, 2007.
- Jungclauss, J. H., Keenlyside, N., Botzet, M., Haak, H., Luo, J. J., Latif, M., Marotzke, J., Mikolajewicz, U., and Roeckner, E.: Ocean circulation and tropical variability in the coupled model ECHAM5/MPI-OM, *J. Climate*, 19, 3952–3972, 2006.
- Kim, S. T. and O’Neil, J. R.: Equilibrium and nonequilibrium oxygen isotope effects in synthetic carbonates, *Geochim. Cosmochim. Ac.*, 61, 3461–3475, 1997.
- Knorr, G., Butzin, M., Micheels, A., and Lohmann, G.: A warm Miocene climate at low atmospheric CO₂ levels, *Geophys. Res. Lett.*, 38, L20701, doi:10.1029/2011GL048873, 2011.

- Kucera, M., Rosell-Mele, A., Schneider, R., Waelbroeck, C., and Weinelt, M.: Multiproxy approach for the reconstruction of the glacial ocean surface (MARGO), *Quaternary Sci. Rev.*, 24, 813–819, doi:10.1016/j.quascirev.2004.07.017, 2005.
- Kurita, N., Noone, D., Risi, C., Schmidt, G. A., Yamada, H., and Yoneyama, K.: Intraseasonal isotopic variation associated with the Madden–Julian Oscillation, *J. Geophys. Res.-Atmos.*, 116, D24101, doi:10.1029/2010JD015209, 2011.
- Lainé, A., Nakamura, H., Nishii, K., and Miyasaka, T.: A diagnostic study of future evaporation changes projected in CMIP5 climate models, *Clim. Dynam.*, 42, 2745–2761, doi:10.1007/s00382-014-2087-7, 2014.
- Lee, J.-E., Fung, I., DePaolo, D. J., and Henning, C. C.: Analysis of the global distribution of water isotopes using the NCAR atmospheric general circulation model, *J. Geophys. Res.-Atmos.*, 112, D16306, doi:10.1029/2006JD007657, 2007.
- Lee, J.-E., Fung, I., DePaolo, D. J., and Otto-Bliesner, B.: Water isotopes during the Last Glacial Maximum: New general circulation model calculations, *J. Geophys. Res.*, 113, D19109, doi:10.1029/2008JD009859, 2008.
- Lee, J. E., Pierrehumbert, R., Swann, A., and Lintner, B. R.: Sensitivity of stable water isotopic values to convective parameterization schemes, *Geophys. Res. Lett.*, 36, L23801, doi:10.1029/2009gl040880, 2009.
- LeGrande, A. N. and Schmidt, G. A.: Sources of Holocene variability of oxygen isotopes in paleoclimate archives, *Clim. Past*, 5, 441–455, doi:10.5194/cp-5-441-2009, 2009.
- Lehmann, M. and Siegenthaler, U.: Equilibrium oxygen- and hydrogen-isotope fractionation between ice and water, *J. Glaciol.*, 37, 23–26, 1991.
- Lewis, S. C., LeGrande, A. N., Kelley, M., and Schmidt, G. A.: Water vapour source impacts on oxygen isotope variability in tropical precipitation during Heinrich events, *Clim. Past*, 6, 325–343, doi:10.5194/cp-6-325-2010, 2010.
- Lewis, S. C., LeGrande, A. N., Kelley, M., and Schmidt, G. A.: Modeling insights into deuterium excess as an indicator of water vapor source conditions, *J. Geophys. Res.-Atmos.*, 118, 243–262, doi:10.1029/2012JD017804, 2013.
- Lohmann, G.: Atmospheric and oceanic freshwater transport during weak Atlantic overturning circulation, *Tellus A*, 55, 438–449, 2003.
- Lorius, C., Merlivat, L., Jouzel, J., and Pourchet, M.: 30 000-Year isotope climatic record from Antarctic ice, *Nature*, 280, 644–648, 1979.
- Macdonald, R. W., Paton, D. W., Carmack, E. C., and Omstedt, A.: The fresh-water budget and under-ice spreading of Mackenzie River water in the Canadian Beaufort Sea based on salinity and ¹⁸O/¹⁶O measurements in water and ice, *J. Geophys. Res.*, 100, 895–919, doi:10.1029/94JC02700, 1995.
- Maher, B. A. and Thompson, R.: Oxygen isotopes from Chinese caves: records not of monsoon rainfall but of circulation regime, *J. Quaternary Sci.*, 27, 615–624, doi:10.1002/jqs.2553, 2012.
- Majoube, M.: Fractionnement en oxygène 18 et en deutérium entre l’eau et sa vapeur, *Journal de Chimie et Physique*, 68, 1423–1436, 1971.
- MARGO Project Members: Constraints on the magnitude and patterns of ocean cooling at the Last Glacial Maximum, *Nat. Geosci.*, 2, 127–132, doi:10.1038/Ngeo411, 2009.
- Marsland, S. J., Haak, H., Jungclaus, J. H., Latif, M., and Roske, F.: The Max-Planck-Institute global ocean/sea ice model with orthogonal curvilinear coordinates, *Ocean Model.*, 5, 91–127, 2003.
- Masson-Delmotte, V., Jouzel, J., Landais, A., Stiévenard, M., Johnsen, S. J., White, J. W. C., Werner, M., Sveinbjornsdottir, A., and Fuhrer, K.: GRIP deuterium excess reveals rapid and orbital-scale changes in Greenland moisture origin, *Science*, 309, 118–121, 2005.
- Masson-Delmotte, V., Kageyama, M., Braconnot, P., Charbit, S., Krinner, G., Ritz, C., Guilyardi, E., Jouzel, J., Abe-Ouchi, A., Crucifix, M., Gladstone, R. M., Hewitt, C. D., Kitoh, A., LeGrande, A. N., Marti, O., Merkel, U., Motoi, T., Ohgaito, R., Otto-Bliesner, B., Peltier, W. R., Ross, I., Valdes, P. J., Vettoretti, G., Weber, S. L., Wolk, F., and Yu, Y.: Past and future polar amplification of climate change: climate model intercomparisons and ice-core constraints, *Clim. Dynam.*, 26, 513–529, doi:10.1007/S00382-005-0081-9, 2006.
- Merlivat, L. and Jouzel, J.: Global climatic interpretation of the deuterium-oxygen 18 relationship for precipitation, *J. Geophys. Res.*, 84, 5029–5033, 1979.
- Meyer, H., Opel, T., Laepple, T., Dereviagin, A. Y., Hoffmann, K., and Werner, M.: Long-term winter warming trend in the Siberian Arctic during the mid- to late Holocene, *Nat. Geosci.*, 8, 122–125, doi:10.1038/ngeo2349, 2015.
- NEEM community members: Eemian interglacial reconstructed from a Greenland folded ice core, *Nature*, 493, 489–494, doi:10.1038/nature11789, 2013.
- North Greenland Ice Core Project members: High-resolution record of Northern Hemisphere climate extending into the last interglacial period, *Nature*, 431, 147–151, doi:10.1038/Nature02805, 2004.
- Paul, A., Mulitza, S., and Pätzold, J.: Simulation of oxygen isotopes in a global ocean model, in: *Use of proxies in paleoceanography: examples from the South Atlantic*, edited by: Fisher, G. and Weller, G., 655–686, Springer, Berlin, Heidelberg, Germany, 1999.
- Pfahl, S. and Sodemann, H.: What controls deuterium excess in global precipitation?, *Clim. Past*, 10, 771–781, doi:10.5194/cp-10-771-2014, 2014.
- Raddatz, T. J., Reick, C. H., Knorr, W., Kattge, J., Roeckner, E., Schnur, R., Schnitzler, K. G., Wetzell, P., and Jungclaus, J.: Will the tropical land biosphere dominate the climate-carbon cycle feedback during the twenty-first century? *Clim. Dynam.*, 29, 565–574, doi:10.1007/S00382-007-0247-8, 2007.
- Risi, C., Bony, S., Vimeux, F., and Jouzel, J.: Water-stable isotopes in the LMDZ4 general circulation model: Model evaluation for present-day and past climates and applications to climatic interpretations of tropical isotopic records, *J. Geophys. Res.-Atmos.*, 115, D12118, doi:10.1029/2009JD013255, 2010a.
- Risi, C., Bony, S., Vimeux, F., Frankenberg, C., Noone, D., and Worden, J.: Understanding the Sahelian water budget through the isotopic composition of water vapor and precipitation, *J. Geophys. Res.*, 115, D24110, doi:10.1029/2010JD014690, 2010b.
- Risi, C., Landais, A., Winkler, R., and Vimeux, F.: Can we determine what controls the spatio-temporal distribution of d-excess and ¹⁷O-excess in precipitation using the LMDZ general circulation model?, *Clim. Past*, 9, 2173–2193, doi:10.5194/cp-9-2173-2013, 2013.

- Roche, D., Paillard, D., Ganopolski, A., and Hoffmann, G.: Oceanic oxygen-18 at the present day and LGM: equilibrium simulations with a coupled climate model of intermediate complexity, *Earth Planet. Sc. Lett.*, 218, 317–330, doi:10.1016/S0012-821x(03)00700-3, 2004.
- Roche, D. M. and Caley, T.: $\delta^{18}\text{O}$ water isotope in the iLOVECLIM model (version 1.0) – Part 2: Evaluation of model results against observed $\delta^{18}\text{O}$ in water samples, *Geosci. Model Dev.*, 6, 1493–1504, doi:10.5194/gmd-6-1493-2013, 2013.
- Roche, D. M., Paillard, D., Caley, T., and Waelbroeck, C.: LGM hosing approach to Heinrich Event 1: results and perspectives from data–model integration using water isotopes, *Quaternary Sci. Rev.*, 106, 247–261, doi:10.1016/j.quascirev.2014.07.020, 2014.
- Roeckner, E., Bauml, G., Bonaventura, L., Brokopf, R., Esch, M., Giorgetta, M., Hagemann, S., Kirchner, I., Kornblueh, L., Manzini, E., Rhodin, A., Schlese, U., Schulzweida, U., and Tompkins, A.: The general circulation model ECHAM5. Part I: Model description, Max Planck Institute for Meteorology, Hamburg, Germany, 2003.
- Roeckner, E., Brokopf, R., Esch, M., Giorgetta, M., Hagemann, S., Kornblueh, L., Manzini, E., Schlese, U., and Schulzweida, U.: Sensitivity of simulated climate to horizontal and vertical resolution in the ECHAM5 atmosphere model, *J. Climate*, 19, 3771–3791, 2006.
- Rozanski, K., Araguas-Araguas, L., and Gonfiantini, R.: Relation between long-term trends of ^{18}O isotope composition of precipitation and climate, *Science*, 258, 981–985, 1992.
- Schäfer-Neth, C. and Paul, A.: Gridded Global LGM SST and Salinity Reconstruction, IGBP PAGES/World Data Center for Paleoclimatology, Boulder. Data Contribution Series #2003-046, NOAA/NGDC Paleoclimatology Program, Boulder CO, USA, available at: ftp://ftp.ncdc.noaa.gov/pub/data/paleo/contributions_by_author/paul2003 (last access: 15 May 2015), 2003.
- Schäfer-Neth, C. and Paul, A.: The Atlantic Ocean at the Last Glacial Maximum: 1. Objective mapping of the GLAMAP sea-surface conditions, in: *The South Atlantic in the late Quaternary – material budget and current systems*, edited by: Wefer, G., Mulitza, S., and Ratmeyer, V., Springer, Berlin, Heidelberg, Germany, 531–548, 2003b.
- Schmidt, G. A.: Oxygen-18 variations in a global ocean model, *Geophys. Res. Lett.*, 25, 1201–1204, 1998.
- Schmidt, G. A.: Forward modeling of carbonate proxy data from planktonic foraminifera using oxygen isotope tracers in a global ocean model, *Paleoceanography*, 14, 482–497, 1999.
- Schmidt, G. A., Bigg, G. R., and Rohling, E. J.: Global seawater oxygen-18 database, available at: <http://www.giss.nasa.gov/data/o18data> (last access: 15 May 2015), 1999.
- Schmidt, G. A., LeGrande, A. N., and Hoffmann, G.: Water isotope expressions of intrinsic and forced variability in a coupled ocean-atmosphere model, *J. Geophys. Res.*, 112, D10103, doi:10.1029/2006jd007781, 2007.
- Schrag, D. P., Adkins, J. F., McIntyre, K., Alexander, J. L., Hodell, D. A., Charles, C. D., and McManus, J. F.: The oxygen isotopic composition of seawater during the Last Glacial Maximum, *Quaternary Sci. Rev.*, 21, 331–342, doi:10.1016/S0277-3791(01)00110-X, 2002.
- Shackleton, N. J.: Attainment of isotopic equilibrium between ocean water and the benthonic foraminifera genus *Uvigerina*: isotopic changes in the ocean during the last glacial, *Gif-sur-Yvette, Colloque international du CNRS*, 219, 203–210, 1974.
- Shah, A. M., Morrill, C., Gille, E. P., Gross, W. S., Anderson, D. M., Bauer, B. A., Buckner, R., and Hartman, M.: Global speleothem oxygen isotope measurements since the Last Glacial Maximum, *Dataset Papers in Science*, 2013, 548048, doi:10.7167/2013/548048, 2013.
- Sharp, Z.: *Principles of Stable Isotope Geochemistry*, Pearson Prentice Hall, Upper Saddle River, New Jersey, USA, 2007.
- Steen-Larsen, H. C., Johnsen, S. J., Masson-Delmotte, V., Stenni, B., Risi, C., Sodemann, H., Balslev-Clausen, D., Blunier, T., Dahl-Jensen, D., Ellehøj, M. D., Falourd, S., Grindsted, A., Gkinis, V., Jouzel, J., Popp, T., Sheldan, S., Simonsen, S. B., Sjolte, J., Steffensen, J. P., Sperlich, P., Sveinbjörnsdóttir, A. E., Vinther, B. M., and White, J. W. C.: Continuous monitoring of summer surface water vapor isotopic composition above the Greenland Ice Sheet, *Atmos. Chem. Phys.*, 13, 4815–4828, doi:10.5194/acp-13-4815-2013, 2013.
- Steen-Larsen, H. C., Masson-Delmotte, V., Hirabayashi, M., Winkler, R., Satow, K., Prié, F., Bayou, N., Brun, E., Cuffey, K. M., Dahl-Jensen, D., Dumont, M., Guillevic, M., Kipfstuhl, S., Landais, A., Popp, T., Risi, C., Steffen, K., Stenni, B., and Sveinbjörnsdóttir, A. E.: What controls the isotopic composition of Greenland surface snow?, *Clim. Past*, 10, 377–392, doi:10.5194/cp-10-377-2014, 2014a.
- Steen-Larsen, H. C., Sveinbjörnsdóttir, A. E., Peters, A. J., Masson-Delmotte, V., Guishard, M. P., Hsiao, G., Jouzel, J., Noone, D., Warren, J. K., and White, J. W. C.: Climatic controls on water vapor deuterium excess in the marine boundary layer of the North Atlantic based on 500 days of in situ, continuous measurements, *Atmos. Chem. Phys.*, 14, 7741–7756, doi:10.5194/acp-14-7741-2014, 2014b.
- Steen-Larsen, H. C., Sveinbjörnsdóttir, A. E., Jonsson, T., Ritter, F., Bonne, J. L., Masson-Delmotte, V., Sodemann, H., Blunier, T., Dahl-Jensen, D., and Vinther, B. M.: Moisture sources and synoptic to seasonal variability of North Atlantic water vapor isotopic composition, *J. Geophys. Res.-Atmos.*, 120, 5757–5774, doi:10.1002/2015JD023234, 2015.
- Stenni, B., Masson-Delmotte, V., Johnsen, S., Jouzel, J., Longinelli, A., Monnin, E., Rothlisberger, R., and Selmo, E.: An oceanic cold reversal during the last deglaciation, *Science*, 293, 2074–2077, 2001.
- Stenni, B., Masson-Delmotte, V., Selmo, E., Oerter, H., Meyer, H., Rothlisberger, R., Jouzel, J., Cattani, O., Falourd, S., Fischer, H., Hoffmann, G., Iacumin, P., Johnsen, S. J., Minster, B., and Udisti, R.: The deuterium excess records of EPICA Dome C and Dronning Maud Land ice cores (East Antarctica), *Quaternary Sci. Rev.*, 29, 146–159, doi:10.1016/J.Quascirev.2009.10.009, 2010.
- Stepanek, C. and Lohmann, G.: Modelling mid-Pliocene climate with COSMOS, *Geosci. Model Dev.*, 5, 1221–1243, doi:10.5194/gmd-5-1221-2012, 2012.
- Tan, M.: Circulation effect: response of precipitation $\delta^{18}\text{O}$ to the ENSO cycle in monsoon regions of China, *Clim. Dynam.*, 42, 1067–1077, doi:10.1007/s00382-013-1732-x, 2014.
- Thompson, L. G., Mosley-Thompson, E., Davis, M. E., Bolzan, J. F., Dai, J., Yao, T., Gundestrup, N. S., Wu, X., Klein, L., and Xie,

- Z.: Holocene–Late Pleistocene climatic ice core records from Qinghai–Tibetan Plateau, *Science*, 246, 474–477, 1989.
- Thompson, L. G., Mosley-Thompson, E., Davis, M. E., Lin, P. N., Henderson, K. A., Coledai, J., Bolzan, J. F., and Liu, K. B.: Late glacial stage and Holocene tropical ice core records From Huascarán, Peru, *Science*, 269, 46–50, 1995.
- Thompson, L. G., Davis, M. E., Mosley-Thompson, E., Sowers, T. A., Henderson, K. A., Zagorodnov, V. S., Lin, P. N., Mikhalevko, V. N., Campen, R. K., Bolzan, J. F., Cole-Dai, J., and Francou, B.: A 25 000-year tropical climate history from Bolivian ice cores, *Science*, 282, 1858–1864, 1998.
- Thompson, L. G., Mosley-Thompson, E., Davis, M. E., Henderson, K. A., Brecher, H. H., Zagorodnov, V. S., Mashiotto, T. A., Lin, P. N., Mikhalevko, V. N., Hardy, D. R., and Beer, J.: Kilimanjaro ice core records: Evidence of Holocene climate change in tropical Africa, *Science*, 298, 589–593, 2002.
- Tian, L., Yao, T., Schuster, P. F., White, J. W. C., Ichiyanagi, K., Pendall, E., Pu, J., and Wu, Y.: Oxygen-18 concentrations in recent precipitation and ice cores on the Tibetan Plateau, *J. Geophys. Res.-Atmos.*, 108, 4293, doi:10.1029-2002JD002173, 2003.
- Tindall, J. C., Valdes, P. J., and Sime, L. C.: Stable water isotopes in HadCM3: Isotopic signature of El Niño Southern Oscillation and the tropical amount effect, *J. Geophys. Res.*, 114, D04111, doi:10.1029/2008jd010825, 2009.
- Uemura, R., Masson-Delmotte, V., Jouzel, J., Landais, A., Motoyama, H., and Stenni, B.: Ranges of moisture-source temperature estimated from Antarctic ice cores stable isotope records over glacial–interglacial cycles, *Clim. Past*, 8, 1109–1125, doi:10.5194/cp-8-1109-2012, 2012.
- Valcke, S., Caubel, A., Declat, D., and Terray, L.: OASIS3 Users's Guide, CERFACS, Toulouse, France, 2003.
- Vimeux, F., Masson, V., Jouzel, J., Stievenard, M., and Petit, J. R.: Glacial–interglacial changes in ocean surface conditions in the southern hemisphere, *Nature*, 398, 410–413, 1999.
- Vimeux, F., Gallaire, R., Bony, S., Hoffmann, G., and Chiang, J.: What are the climate controls on δD in precipitation in the Zongo Valley (Bolivia)? Implications for the Illimani ice core interpretation, *Earth Planet. Sc. Lett.*, 240, 205–220, doi:10.1016/j.epsl.2005.09.031, 2005.
- Wackerbarth, A., Scholz, D., Fohlmeister, J., and Mangini, A.: Modelling the $\delta^{18}O$ value of cave drip water and speleothem calcite, *Earth Planet. Sc. Lett.*, 299, 387–397, doi:10.1016/j.epsl.2010.09.019, 2010.
- WAIS Divide Project Members: Onset of deglacial warming in West Antarctica driven by local orbital forcing, *Nature*, 500, 440–444, doi:10.1038/nature12376, 2013.
- Wang, Y., Cheng, H., Edwards, R. L., Kong, X., Shao, X., Chen, S., Wu, J., Jiang, X., Wang, X., and An, Z.: Millennial- and orbital-scale changes in the East Asian monsoon over the past 224 000 years, *Nature*, 451, 1090–1093, doi:10.1038/Nature06692, 2008.
- Wang, Y. J., Cheng, H., Edwards, R. L., An, Z. S., Wu, J. Y., Shen, C. C., and Dorale, J. A.: A High-Resolution Absolute-Dated Late Pleistocene Monsoon Record from Hulu Cave, China, *Science*, 294, 2345–2348, doi:10.1126/science.1064618, 2001.
- Wei, W. and Lohmann, G.: Simulated Atlantic multidecadal oscillation during the Holocene, *J. Climate*, 25, 6989–7002, doi:10.1175/JCLI-D-11-00667.1, 2012.
- Wei, W., Lohmann, G., and Dima, M.: Distinct modes of internal variability in the global meridional overturning circulation associated with the Southern Hemisphere westerly winds, *J. Phys. Oceanogr.*, 42, 785–801, doi:10.1175/JPO-D-11-038.1, 2012.
- Werner, M. and Heimann, M.: Modeling interannual variability of water isotopes in Greenland and Antarctica, *J. Geophys. Res.*, 107, 4001, doi:10.1029/2001JD900253, 2002.
- Werner, M., Mikolajewicz, U., Heimann, M., and Hoffmann, G.: Borehole vs. isotope temperatures on Greenland: Seasonality does matter, *Geophys. Res. Lett.*, 27, 723–726, 2000.
- Werner, M., Heimann, M., and Hoffmann, G.: Isotopic composition and origin of polar precipitation in present and glacial climate simulations, *Tellus B*, 53, 53–71, 2001.
- Werner, M., Langebroek, P. M., and Carlsen, T.: Stable water isotopes in the ECHAM5 general circulation model: Toward high-resolution isotope modeling on a global scale, *J. Geophys. Res.-Atmos.*, 116, D15109, doi:10.1029/2011jd015681, 2011.
- Xu, X.: Variations of oceanic and foraminiferal oxygen isotopes at the present day and the Last Glacial Maximum: Equilibrium simulations with an oceanic general circulation model, Universität Bremen, Alfred-Wegener-Institut, available from: <http://epic.awi.de/32264/> (last access: 15 May 2015), 2012.
- Xu, X., Werner, M., Butzin, M., and Lohmann, G.: Water isotope variations in the global ocean model MPI-OM, *Geosci. Model Dev.*, 5, 809–818, doi:10.5194/gmd-5-809-2012, 2012.
- Yao, T., Thompson, L., Yang, W., Yu, W., Gao, Y., Guo, X., Yang, X., Duan, K., Zhao, H., Xu, B., Pu, J., Lu, A., Xiang, Y., Kattel, D. B., and Joswiak, D.: Different glacier status with atmospheric circulations in Tibetan Plateau and surroundings, *Nat. Clim. Change*, 2, 663–667, doi:10.1038/nclimate1580, 2012.
- Zaucker, F. and Broecker, W. S.: The influence of atmospheric moisture transport on the fresh water balance of the Atlantic drainage basin: General circulation model simulations and observations, *J. Geophys. Res.*, 97, 2765–2773, doi:10.1029/91JD01699, 1992.
- Zhang, X., Lohmann, G., Knorr, G., and Xu, X.: Different ocean states and transient characteristics in Last Glacial Maximum simulations and implications for deglaciation, *Clim. Past*, 9, 2319–2333, doi:10.5194/cp-9-2319-2013, 2013.
- Zhang, X., Lohmann, G., Knorr, G., and Purcell, C.: Abrupt glacial climate shifts controlled by ice sheet changes, *Nature*, 512, 290–294, doi:10.1038/nature13592, 2014.
- Zhuang, K. and Giardini, J. R.: Ocean cooling pattern at the Last Glacial Maximum, *Advances in Meteorology*, 2012, 213743, doi:10.1155/2012/213743, 2012.